International Journal of Solids and Structures 60–61 (2015) 107–124

Contents lists available at ScienceDirect

International Journal of Solids and Structures

journal homepage: www.elsevier.com/locate/ijsolstr

Mechanical response of Ti–6Al–4V octet-truss lattice structures

Liang Dong [a,*], Vikram Deshpande [b], Haydn Wadley [a]

[a] Department of Materials Science and Engineering, University of Virginia, Charlottesville, VA 22903, United States
[b] Engineering Department, Trumpington Street, University of Cambridge, UK

ARTICLE INFO

Article history:
Received 11 December 2014
Received in revised form 8 January 2015
Available online 19 February 2015

Keywords:
Octet-truss lattice
Elastic stiffness
Strength
Titanium alloys

ABSTRACT

A simple snap-fit and vacuum brazing method has been developed to fabricate three dimensional space filling octet-truss lattice structures from Ti–6Al–4V alloy sheets. Using strut lengths of 7–25 mm resulted in a relative density of the lattices ranging from 2% to 16%. The lattice elastic stiffness constants and strengths have been characterized under through-thickness compression and in-plane shear as a function of their relative density, and are shown to be well predicted by previously proposed micromechanical models adapted to account for the increased nodal mass and strut separations of the snap-fit lattice design. The Ti–6Al–4V octet-truss lattices exhibit excellent mechanical properties compared to other cellular material – cell topology combinations, and appear to be promising candidates for high temperature applications where a robust mechanical performance is required.

1. Introduction

There are many ways to create 3D space filling cellular materials. Periodic cellular structures, are constructed from unit cells with honeycomb (Bitzer, 1997; Wadley, 2003, 2006; Dharmasena, 2008; Russell et al., 2008), tetrahedral (Sypeck, 2002; Kooistra, 2004, 2007; Lim and Kang, 2006), 3D Kagome (Lim and Kang, 2006; Lee et al., 2007; Park et al., 2011), octet truss (Bitzer, 1997; Fuller, 1961) and pyramidal (Kooistra, 2007; Queheillalt, 2005; Finnegan et al., 2007; Queheillalt et al., 2008) arrangements of webs or struts. Tetrahedral, pyramidal and 3D Kagome unit cells require struts or webs to connect their out of plane members in order for them to become statically determinant, stretch-dominated structures (Deshpande et al., 2001). Space filling, structurally efficient lattices can then be constructed by the assembly of these unit cells in three dimensions. These statically determinate lattice structures can act as a material in the sense that their properties are independent of the size of the sample, provided its exterior dimensions are large compared to those of its cells. However, in some sandwich panel applications (Sypeck, 2002; Kooistra, 2004, 2007; Wang et al., 2003) it may be preferable to use only the out of plane webs or struts to maintain separation of the face sheets while utilizing the faces to ensure unit cell static determinacy. Foams made from polymers, metals or ceramics with interconnected or closed cells also provide a means for filling space with a random arrangement of cells (San Marchi et al., 2002). However, their cells have a variable (but low) strut or web nodal connectivity, and are bending dominated structures with moduli and strengths that decrease rapidly as the fraction of solid material (their relative density) is decreased (Deshpande et al., 2001).

Lattice structures with open cell intermediate face sheets between the layers of inclined struts, such as the octet-truss lattice (Bitzer, 1997; Fuller, 1961), have attracted considerable recent interest since they are structurally more efficient than foams of a similar density made from the same material. Recent casting approaches have demonstrated the possibility of making octet-truss lattices with strut lengths in the 5–10 mm range (Deshpande et al., 2001), while self-propagating waveguide or laser based stereo-lithographic methods, when combined with electroless nickel plating or vapor deposition have enabled fabrication of micrometer scale structures (Torrents et al., 2012; Zheng et al., 2014; Bauer et al., 2014) offering opportunities to exploit other functionalities of materials available in the small length scale limit.

An octet-truss lattice structure is illustrated in Fig. 1, and was first proposed by Fuller (1961), as a method for filling 3D space with a structurally efficient truss structure of arbitrary cell size. Its nodes form a face centered cubic structure, Fig. 1(b). Since the structure has a high nodal connectivity of 12, its mechanical response is stretch-dominated (Deshpande et al., 2001). When made from high specific modulus and strength materials, the octet-truss lattice is therefore a weight efficient, stress supporting cellular topology, with a stiffness and strength predicted to scale linearly with relative density, $\bar{\rho}$ (the density of the structure divided by that of the material from which it is made) (Wadley, 2006).

* Corresponding author. Tel.: +1 434 982 5678.
E-mail address: ld5fy@virginia.edu (L. Dong).

http://dx.doi.org/10.1016/j.ijsolstr.2015.02.020
0020-7683/

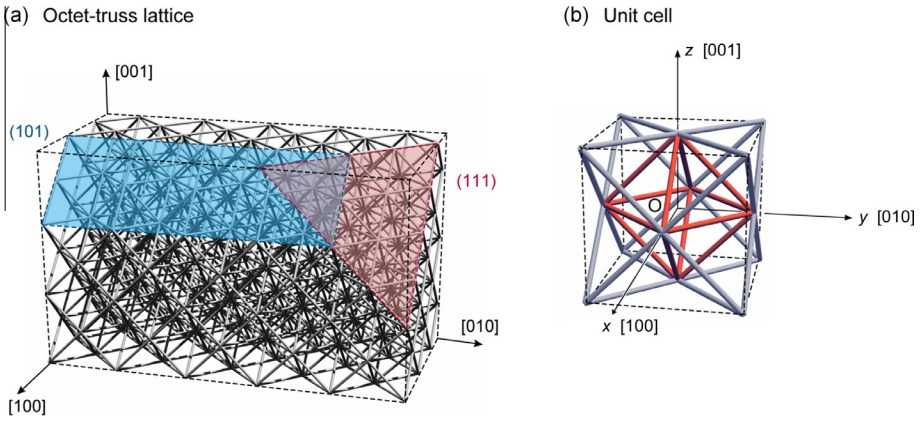

Fig. 1. (a) An octet-truss lattice constructed by the 3D packing of unit cells. (b) A unit cell of the face centered cubic crystal symmetry octet-truss lattice is composed of a central octahedral cell constructed with 12 struts that is bounded by 8 edge tetrahedrons. Each node within the octet lattice lies at the intersection of 12 struts.

Material property charts are a useful way to compare the mechanical properties of low density materials. Fig. 2 shows the density dependent modulus and strength under compressive loading for low density foams (polymer, metal and alumina) and space filling lattice structures made from investment cast Al–7Si–0.3Mg (Deshpande et al., 2001), Ti–6Al–4V and Ti–6Al–2Sn–4Zr–2Mo alloys (Li et al., 2008a,b), similar structures made by electrodeposition of Ni–7P (Torrents et al., 2012; Zheng et al., 2014), from carbon fiber laminate composites (Cheung and Gershenfeld, 2013), photosensitive HDDA polymers (Zheng et al., 2014), and by the vapor deposition of alumina (Zheng et al., 2014; Bauer et al., 2014). The moduli and strengths of both foams and lattices scale with those of the materials from which they are made (Gibson and Ashby, 1999; Ashby, 2000), but foams are substantially more compliant and weaker than lattice topology counterparts (made with the same density and material) for reasons identified above.

Octet-truss lattice structures made from low density metal alloys with strut diameters in the millimeter range are potential candidates for stress supporting aerospace applications. Lightweight aluminum alloy octet-truss lattice structures have been made by an investment casting (Deshpande et al., 2001) and by 3D additive manufacturing methods (Rosen, 2007; Chu et al., 2010; Williams et al., 2011). However, these processes remain difficult to implement with the highest strength to weight ratio alloys of aerospace interest. There is particular interest in making octet-truss structures from titanium alloys since their strength to weight ratio is approximately twice that of aluminum alloys. Many titanium alloys can also be used at continuous service temperatures well above the limits of other light metal alloys based on aluminum or magnesium (Kulekci, 2008; Ye, 2003). Some titanium alloys also have excellent corrosion resistance, and are therefore widely used in chemical processing equipment (Couper et al., 2009), and heat exchangers (Lu et al., 1998; Boomsma et al., 2003). The Ti–6Al–4V alloy is the most widely used titanium alloy, and accounts for more than 50% of total titanium usage. Its uses include aircraft turbine engine and structural components, fasteners, high performance automotive parts, and a variety of marine applications (Boyer et al., 1993; Ritchie et al., 1999; Brewer et al., 1998; Boyer and Briggs, 2005; Froes et al., 2004; Gorynin, 1999).

Titanium alloy lattice structures have been fabricated with aerospace-quality investment casting techniques (Li et al., 2008a,b). While this approach has the potential to enable fabrication of complex shaped structures, it is costly to implement, and requires development of methods to detect and repair the casting defects often present in investment cast lattice structures (Wang et al., 2003). Because of the cost and complexity of the titanium investment fabrication process, there is very limited mechanical property data for titanium-based lattice structures as a function of their relative density, Fig. 2.

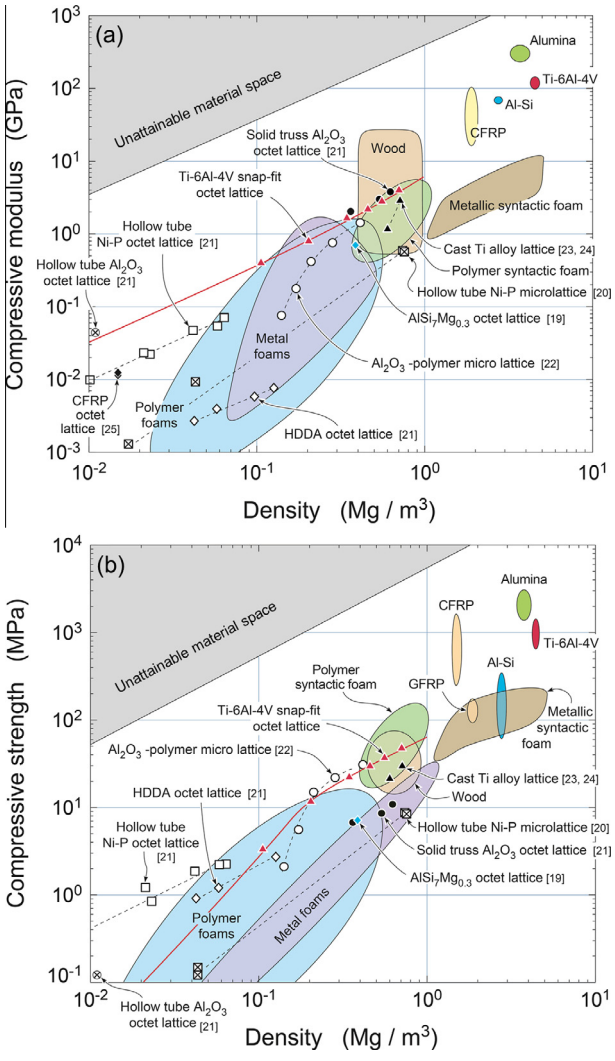

Fig. 2. Material property charts comparing material stiffness (a) and strength (b) in compression against density. The experimental data (unit cell response, Table 2) and predicted range of these properties for the Ti–6Al–4V octet-truss lattice structure fabricated here (Ti–6Al–4V snap fit octet lattice) have been included for comparison with other octet lattice truss materials. The grey shaded areas define regions that cannot be reached under ambient conditions.

Here, we explore the use of a simple "snap-fit" method (Finnegan et al., 2007) for fabricating the struts and open face sheets of planar octet-truss structures from thin plate material. This assembly method is combined with vacuum brazing to fabricate octet-truss lattices from a Ti–6Al–4V alloy sheet. The mechanical responses of the titanium octet-truss lattices under compression and shear have been experimentally investigated, and their compressive and shear strengths and moduli determined as a function of lattice density, and compared with micromechanical predictions to evaluate the inter relationships between lattice topology, material properties and relative density.

2. Lattice fabrication, relative density and solid material properties

2.1. Lattice fabrication

The octet-truss lattice structures were fabricated from Ti–6Al–4V sheets of a single thickness, $t = 1.59$ mm, in a three step process summarized schematically in Fig. 3. The truss row patterns, Fig. 3(a), and intermediate (open cell) face sheets, Fig. 3(c), were water jet cut from as-received Ti–6Al–4V sheets forming the geometries shown in the two figures. Rows of trusses were collinearly aligned and a second collinear array, oriented at 90° to the first, was snap-fit attached to their tops forming a [0°/90°] arrangement of trusses enclosing a pyramidal void shape, Fig. 3(b). Control of the slot tolerance in the nodal regions enabled a mechanically stable snap-fitted plane of pyramidal trusses to be assembled in this way. The truss layer planes were then snap-fitted into the crosses of the intermediate face sheet and the process repeated to form the octet-truss lattice, Fig. 3(d). Samples with square cross section trusses of width t, and various lengths, l, were made to enable study of the truss slenderness ratio, t/l, upon mechanical response. The geometric parameters defining the structures assembled for testing are defined in Fig. 4 and their values summarized in Table 1 for each test structure. The maximum gap (determined by the tolerances of the water-jet cutting process) between struts meeting at the nodes was about 90 μm.

The snap-fit lattice was bonded using a vacuum brazing approach. A 40Ti–20Cu–20Ni–20Zr (wt.%) braze alloy (Lucas Milhaupt) was first applied to the nodal regions of the assembled structure. The alloy was applied as a powder carried in a polymer binder. Brazing was accomplished by placing the lattice structures in a high-temperature vacuum brazing furnace and heating at 10 °C/min to 500 °C, holding for 20 min to volatilize and remove the polymer binder from the furnace, and then heating to 900 °C for 30 min at a chamber pressure of $\sim 5 \times 10^{-2}$ Pa. This braze alloy has a solidus temperature of 848 °C. Once melted, it wetted this titanium alloy well, and flowed freely to fill small gaps at the nodes at the brazing temperature used in the study. After brazing, the furnace was cooled at a rate of 45 °C/min, to 600 °C, at which temperature a 20 min annealing was performed to reduce internal residual stress. The furnace was finally cooled to ambient temperature at a rate of 15 °C/min.

The strength of a brazed bond between two plates generally decreases as the gap between them increases. Lap shear test coupons with gaps of ~90 μm were included in the brazing runs and subsequently tested, in accordance with the ASTM D1002 standard, to ensure adequate bond strength was achieved. The measured shear strength of 40Ti–20Cu–20Ni–20Zr bonded Ti–6Al–4V sheets was found to be approximately 450 MPa for a brazed joint gap of about 90 μm.

Photographs taken from several orientations of one of the brazed lattice structures later used for compression testing are shown in Fig. 5. Octet-truss lattice structures for shear testing were also manufactured with solid external face sheets to facilitate gripping in a shear test fixture. Since the in-plane shear response of the octet-truss core is anisotropic, the response is dependent on the direction of shearing. The unit cell sketched in Fig. 4(c) specifies the shearing direction by the angle, $\alpha = 45°$ or 0°. Photographs of the shear samples for testing in both $\alpha = 45°$ and 0° orientations are shown in Fig. 6 during their assembly process so that the orientation of the lattice can be clearly seen. The top row of photographs shows that a two cell wide, octet-truss core, orientated with $\alpha = 45°$ can have either two or three nodal connections with the solid face sheet through which shear loads were applied. Since the number of nodal connections at the edge of a shear sample influences the mechanical response, samples with two edge geometries (identified as Type I and II), were fabricated, and also shown at various stages of assembly in Fig. 6(a) and (b).

2.2. Relative density

A schematic drawing of the octahedral unit cell of the snap-fit lattice is shown in Fig. 4(c) together with coordinate systems used later. It also defines the geometric parameters of the lattice. Note that for the square cross section truss, $t = w$, and we selected a truss inclination angle $\omega = 45°$ to balance the compressive and shear responses of the structure. By calculating the volumes of regions occupied by material, and scaling this by the unit cell volume, the relative density, $\bar{\rho}$ of the octahedral unit cell of the snap-fit octet-truss lattice (including nodal mass contributions) is given by;

$$\bar{\rho} = \frac{6\sqrt{2}lt^2 + \left(K_1 - K_2 t + 2\sqrt{2}t^2\right)t}{(l + K_3)(l + K_4)^2} \tag{1}$$

where,

$$K_1 = \sqrt{2}(b + 2m)^2 + 2\sqrt{2}h(b + c) + 4\sqrt{2}bh_{\text{tab}}$$

$$K_2 = (2\sqrt{2} + 2)b - 2c + 2\sqrt{2}(h + h_{\text{tab}}) + 8m$$

$$K_3 = \sqrt{2}(h + 2h_{\text{tab}}),$$

$$K_4 = \frac{\sqrt{2}}{2}(b + c)$$

and the geometric parameters are defined on Fig. 4.

Eq. (1) was arranged in this way to separate volume contributions from the trusses (first term of the numerator) and nodes. Some further simplification can be achieved by introducing non-dimensional lengths; $\bar{t} = t/l$, $\bar{b} = b/l$, $\bar{c} = c/l$, $\bar{h}_{\text{tab}} = h_{\text{tab}}/l$, $\bar{h} = h/l$ and $\bar{m} = m/l$. As a result, $\bar{K}_1 = K_1/l^2$, $\bar{K}_2 = K_2/l$, $\bar{K}_3 = K_3/l$, and $\bar{K}_4 = K_4/l$, whereupon;

$$\bar{\rho} = \frac{6\sqrt{2}\bar{t}^2 + \left(\bar{K}_1 - \bar{K}_2\bar{t} + 2\sqrt{2}\bar{t}^2\right)\bar{t}}{(1 + \bar{K}_3)(1 + \bar{K}_4)^2} \tag{2}$$

It can be shown that in the limit of vanishing node size, Eq. (1) reduces, in a first order approximation, to the relative density expression for the ideal octet-truss lattice;

$$\bar{\rho}_{\text{oct}} = 6\sqrt{2}\left(\frac{t}{l}\right)^2 \tag{3}$$

Octet-truss lattice structures, with the extra mass of nodal material accounted for, have a relative density given by Eq. (1), and were fabricated with relative densities ranging from 2% to 16% by allowing the strut length l to vary between 7 and 25 mm. All the lattice structures had square cross section struts with a width, w and thickness $t = 1.59$ mm, and node widths defined by $b = 4.76$ mm and

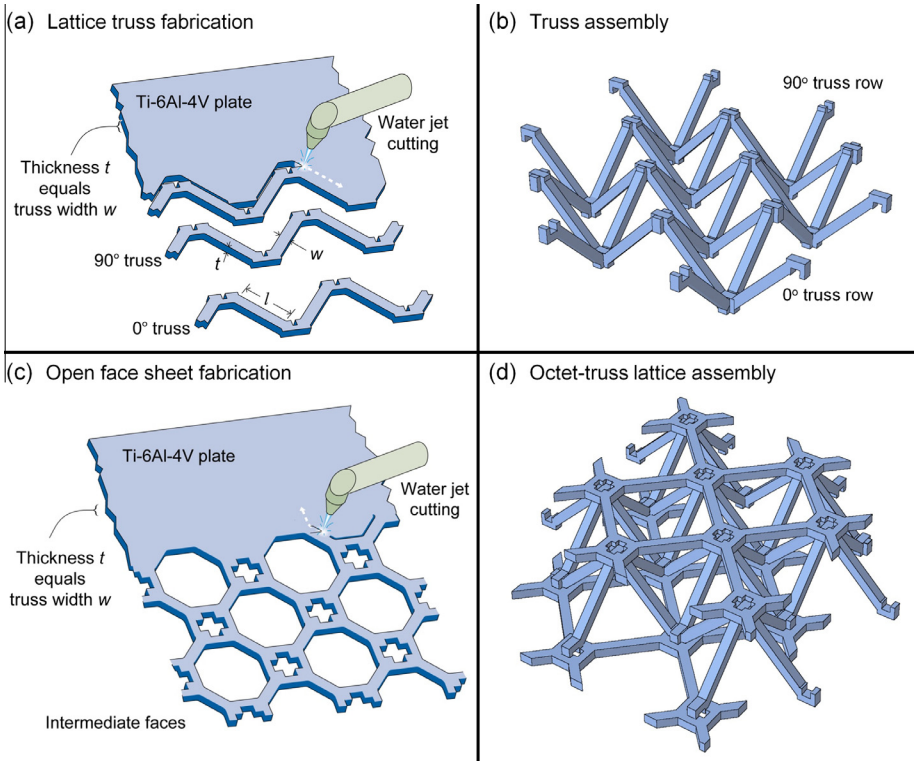

Fig. 3. Schematic illustration of the "snap-fit" truss fabrication and assembly method for making the Ti–6Al–4V octet-truss lattice.

c = 2.24 mm. The relative densities calculated by either Eq. (1) (or by Eq. (3)) ranged from 2.4% (or 3.4%) for the lowest density sample to 15.9% (or 43.3%) for the highest density sample.

2.3. Solid material characterization

A low magnification micrograph of the nodal region of a brazed lattice structure taken in the backscattered electron imaging (BSE) mode[1] is shown in Fig. 7(a). It can be seen that the braze alloy wetted the Ti–6Al–4V base metal and was drawn into both the narrow and wider gaps between the truss members. High magnification views of both narrow and wider gap areas, marked by dashed boxes in Fig. 7(a) at the central bond line are shown in Fig. 7(b) and (c). Since the brazing temperature (900 °C) was below the β-phase transus temperature (980 °C) for the Ti–6Al–4V alloy (Donachie, 2000), the original equiaxed α-grain and intergranular β-phase microstructure of the original alloy was preserved. The average grain diameter of the α-phase was about 7 μm, while the average thickness of the β-phase was less than 1 μm, Fig. 8.

A brazed joint typically consisted of three zones marked 1, 2 and 3, Fig. 7(b). Region 1 was the diffusion zone with a fine Widmanstätten structure in the base alloy near the interface (Onzawa et al., 1990; Botstein and Rabinkin, 1994; Lugscheider and Broich, 1995). Region 2 was a β-titanium rich zone next to the diffusion zone, while region 3 was a brittle intermetallic phase rich zone at the center of the braze filled region (at center of Fig. 7(b)). The central (brittle intermetallic phase rich) zone could be eliminated when the brazing joint clearance was sufficiently small, as shown in Fig. 7(c). In this case, the brazed joint consisted of only the diffusion and β-titanium phase zones with a total thickness of approximately 90 μm. Elemental distribution maps corresponding to regions (b) and (c) of Fig. 7 are shown in Fig. 7(d) and (e) respectively. They show the spatial distribution of the alloy elements (Ti, Al, V) and those of the braze alloy (Zr, Ni, and Cu) for both the narrow and wide gap regions of a braze joint. Substantial lateral diffusion of Zr, Cu and Ni into the titanium alloy had occurred in the narrow clearance region of a joint. However, the intermetallic rich region at the center of the wider gap regions of a joint retained substantial Cu, Zr and Ni from the braze alloy following the brazing recipe used here.

In order to later predict lattice mechanical properties, the uniaxial tensile response of Ti–6Al–4V alloy subjected to the same thermal history as the lattice structures was measured. The tensile response measured at a strain rate of $10^{-4}\,s^{-1}$ is shown in Fig. 9. The elastic (Young's) modulus, E_s and 0.2% offset yield strength, σ_{ys} were 123 GPa and 932 MPa, respectively. The tangent modulus, E_t (given by the slope of the true stress–true strain response of the solid material at the inelastic bifurcation stress, σ_{IE}) was obtained by differentiation of a modified Ramberg–Osgood fit (Rasmussen, 2003) to the measured stress–strain responses. The inelastic bifurcation stress was obtained using the tangent modulus theory (Gere and Timoshenko, 1984; Shanley, 1967) as discussed in Section 4.2.

3. Compression and shear responses

The Ti–6Al–4V octet-truss lattices were tested at ambient temperature in free compression and shear at a nominal strain rate of $3 \times 10^{-4}\,s^{-1}$ in accordance with ASTM standards C365 and C273. The ASTM C273 standard specifies use of a compression shear plate configuration and a length to thickness ratio of the shear sandwich panel larger than 12:1; however, a smaller length to thickness ratio is also acceptable as later clarified by Adams (Adams, 2007). The shear samples used here had a length to thickness ratio of about 4:1. The shear response was also dependent upon the direction of loading with respect to the lattice orientation. Tests were

[1] Lighter grey contrast regions correspond to areas with a higher concentration of high atomic number elements.

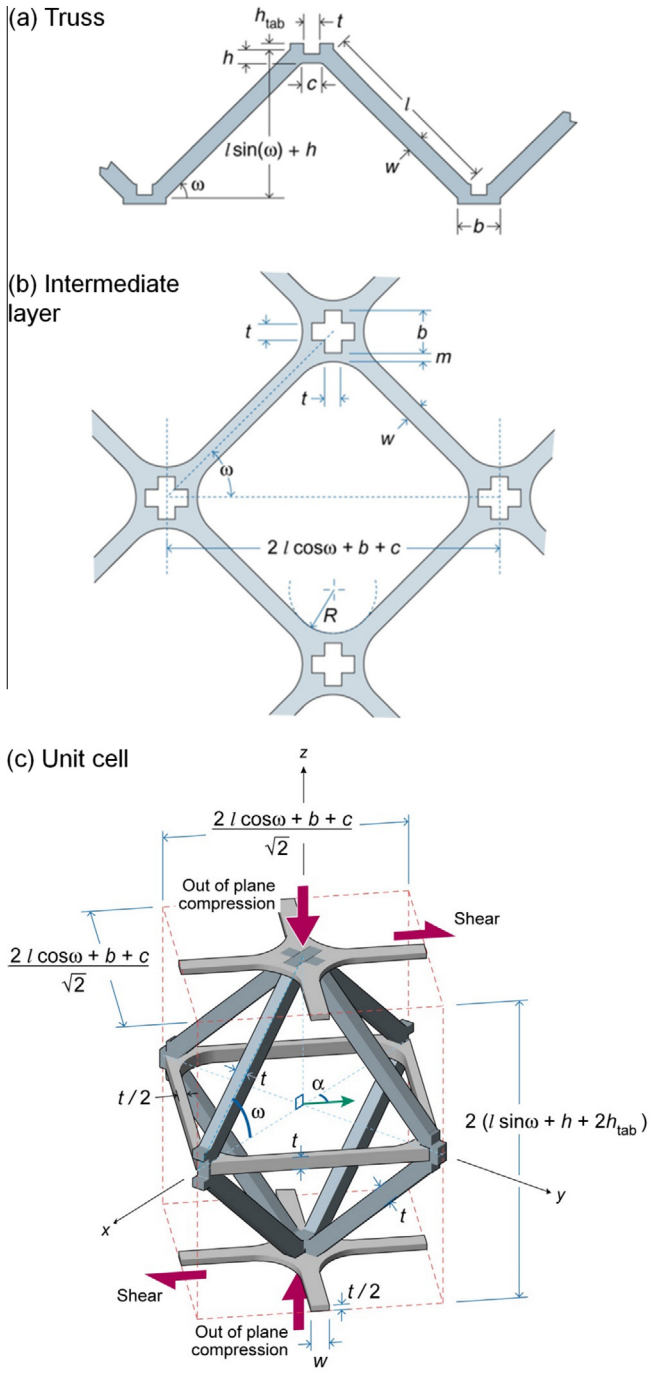

Fig. 4. The geometries with relevant design variables identified of (a) the out of plane trusses and (b) the intermediate truss layer, (c) the unit cell of the snap-fit modified octet-truss lattice with the Cartesian co-ordinate system and loading directions also specified.

therefore conducted at two orientations to determine the two independent in-plane shear tensor strength and modulus components. The measured load cell forces were used to calculate the compressive and shear stresses applied to the structure. The sample side lengths are defined using Figs. 5 and 6, as the distances between the left-and-right edges of the samples while the top-and-bottom edges were defined by the out-of-plane edge struts. The volume occupied by the extra edge nodes was not taken into account since they contribute neither stiffness nor strength (they could be trimmed off if necessary without changing the mechanical response). The loading directions are shown in Fig. 4(c). A laser extensometer measured the compressive strain by monitoring the displacements of the top and bottom perforated intermediate surface layers, and the shear strain by monitoring the displacements of the shear plates. Unloading–reloading cycles were conducted prior to the onset of inelastic deformation in order to determine the elastic stiffness components of the specimens.

3.1. Compression results

The z (through-thickness) direction compressive stress–strain responses of the lattice structures are shown in Fig. 10. The response exhibited characteristics typical of cellular structures including; a region of nominally elastic response, yielding, plastic strain hardening to a peak in strength, followed by a drop in flow stress to a plateau region and finally rapid hardening associated with contact of the deformed struts with each other (densification). In contrast to many foam topology materials, the drop in flow stress after attainment of lattice strength was very large, and indicative of a mechanical instability. Photographs of the lattice structures showing characteristic plastic deformation behaviors in compression are shown in Fig. 11.

The lowest relative density lattice ($\bar{\rho} = 2.4\%$) failed by elastic buckling of the struts. Higher density samples failed by inelastic buckling or yielding of the out-of-plane strut members as the lattice strength was achieved. The out-of-plane struts continued to buckle with increasing plastic strain, which resulted in increased deflection of the struts and asymmetrical loading at the nodes which caused nodal rotation. Strut buckling was accompanied by a significant drop in flow stress. The in-plane struts were also subjected to torsion and bending deformations due to nodal rotations. Lateral (Poisson) expansion of the lattices was also observed during compression without a lateral boundary constraint. Plastic hinges were formed near the middle and two ends of the out-of-plane struts. Truss fracture was finally observed at the plastic hinges of the out-of-plane struts, and for in-plane struts near their nodal connections due to the significant deformation induced by the combined tension, bending and torsion loading in these regions. The buckled trusses eventually contacted each other at the densification strain coincident with rapid hardening of the flow stress versus strain curve. It is noted here that the flow stress dropped quickly after the peak in strength, which indicates less than the ideal energy absorption seen in some other structures (San Marchi et al., 2002; Gibson and Ashby, 1999; Holloman et al., 2013). This effect is attributed to the buckling instability of struts made from a low strain hardening rate (tangent modulus) Ti–6Al–4V alloy. Table 2 summarizes the relative densities (calculated using Eq. (1)), t/l ratios, elastic compressive moduli and compressive strengths of the octet-truss lattice compression specimens.

The octet truss does not have long range buckling modes and so we expect the one layer structure to give representative results for the peak strength. However, post-peak collapse bands may be

Table 1
Node and strut dimensions for the octet-truss lattices used in this study (unit: mm).

t	w	b	c	h	h_{tab}	ω	t_0	m	R
1.588	1.588	4.763	2.235	0.953	1.588	45°	1.270	1.346	5.080

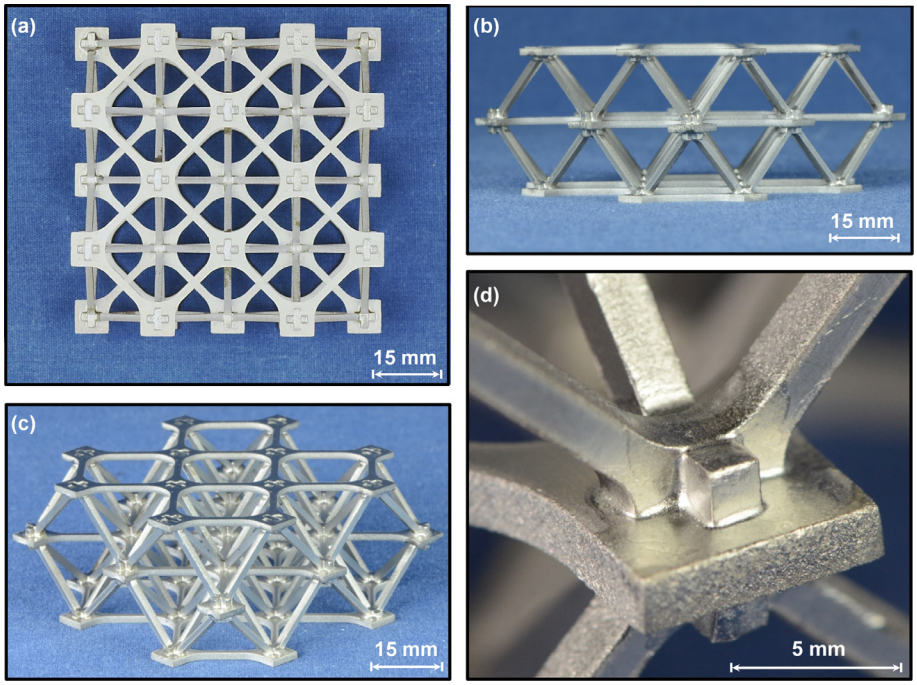

Fig. 5. Photographs of a Ti–6Al–4V octet-truss lattice compression specimen with a relative density of 4.6%; (a) view in the compression loading direction, (b) a side view showing the out-of-plane pyramidal struts and (c) an isometric view. (d) Shows a close-up of a brazed node at the side of the sample where three struts from above and below meet two of the intermediate layer at a sample edge node.

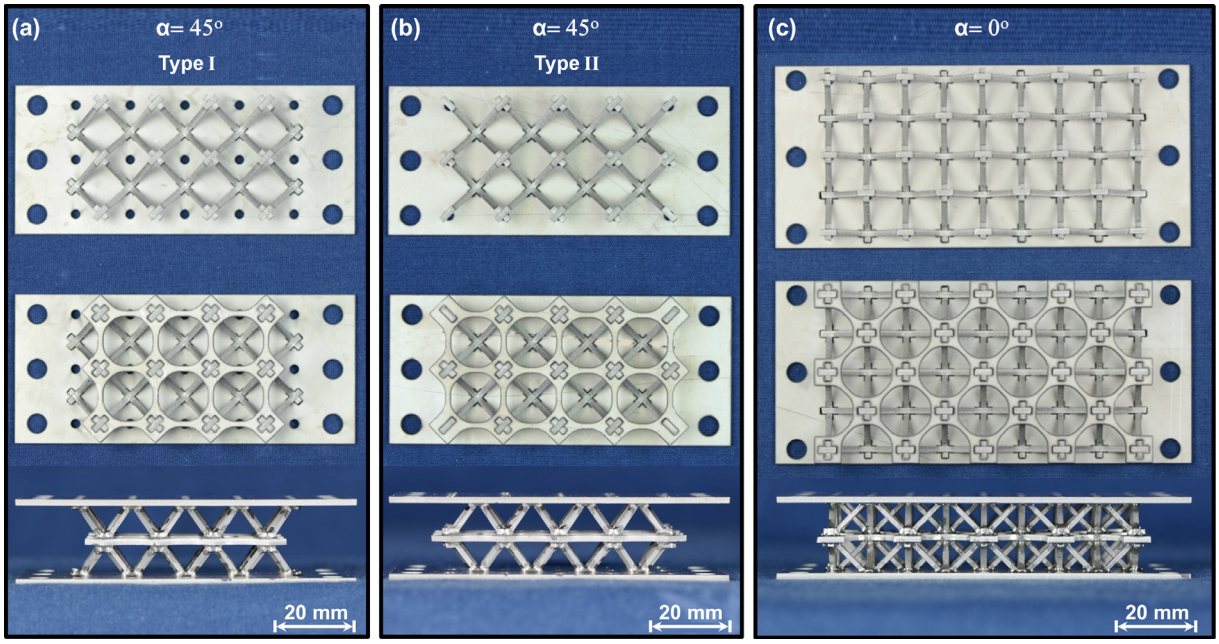

Fig. 6. Photographs of octet-truss shear test structures with a relative density of 10.4%. (a) Corresponds to a Type I sample subsequently loaded at $\alpha = 45°$, (b) to a Type II sample also loaded at $\alpha = 45°$ and (c) is a sample to be tested at $\alpha = 0°$. Photographs of the corresponding disassembled parts before brazing are used to illustrate the internal truss structures.

affected by the specimen size employed and will require investigation in future studies.

3.2. Shear results

The (001) in-plane shear stress–strain responses of the lattice structures are shown in Fig. 12 for $\alpha = 45°$ and 0°. For test orientations with $\alpha = 45°$, each unit cell has four out-of-plane strut members loaded in compression and four in tension; whereas, in the case of shear loading in the $\alpha = 0°$ direction, a unit cell has only two out-of-plane strut members loaded in compression and two in tension. The $\alpha = 45°$ samples were fabricated to investigate the effect of the edge nodal connectivity. The Type I samples had a concave edge truss geometry, Fig. 12(a), while that of the Type II cores was convex, Fig. 12(b). It is evident that an end nodal deflection in the z (through-thickness) direction will occur for $\alpha = 45°$ Type II

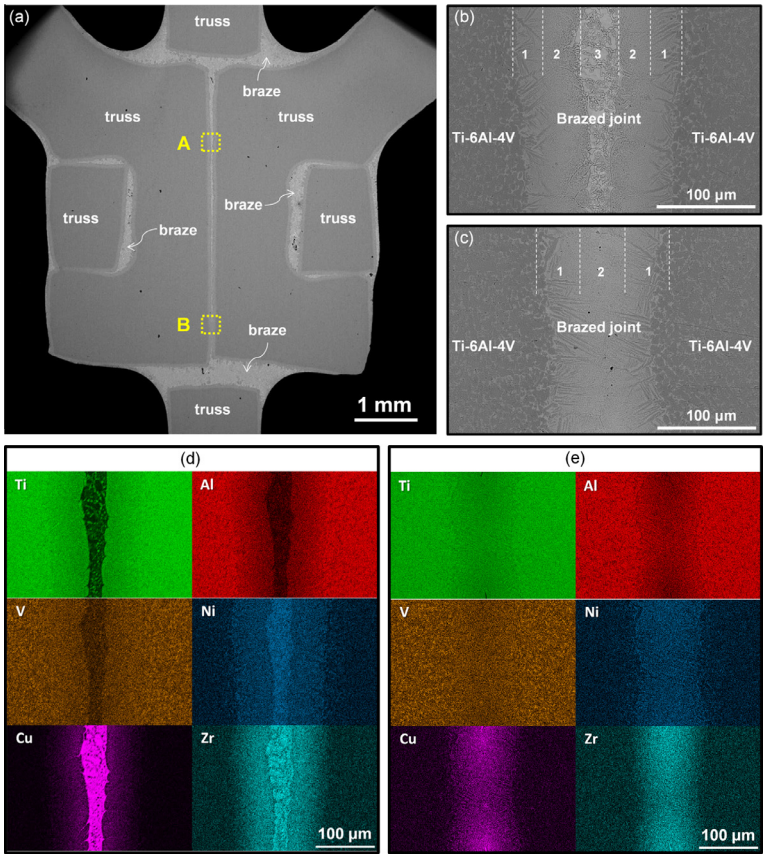

Fig. 7. (a) Cross-sectional SEM image (in BSE contrast mode) through a brazed node. Higher magnification views of the rectangular areas A and B are shown in (b) and (c) respectively. Elemental composition maps are shown for region A in (d) and for region B in (e).

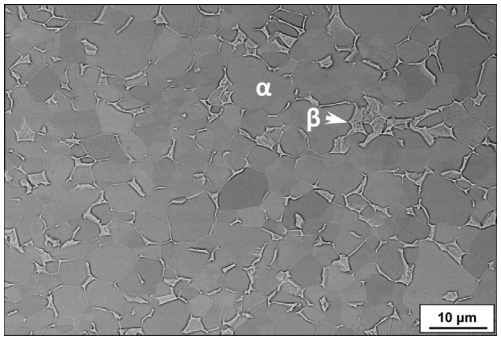

Fig. 8. Microstructure within the Ti–6Al–4V struts after the brazing heat treatment (900 °C, 30 min). The α-phase grain size was approximately 7 μm.

cores and for $\alpha = 0^\circ$ cores under (001) in-plane shear loading. However the end nodes of $\alpha = 45^\circ$ Type I cores are stable under (001) in-plane shear loading.

Most of the samples exhibited stress versus strain responses typical of lattice sandwich cores including elastic behavior during initial loading followed by work hardening until the lattice shear strength was achieved. However, the lowest density sample ($\bar{\rho} = 2.4\%$) failed by elastic buckling of the out-of-plane struts at the peak in flow stress. Samples with higher relative densities initially failed by inelastic buckling or tensile yielding of the out-of-plane struts. Continued loading eventually resulted in fracture of the tensile loaded truss members near their nodes when the lattice shear strength was reached. This was accompanied by an abrupt drop in flow stress. Plastic buckling of some out-of-plane truss members at the ends of the shear samples was observed prior to attainment of the lattice shear strength. This was a manifestation of the compressive loading component of the ASTM C273 test method. Deflection of the edge nodes at the two ends of the shear samples was observed in the cases of $\alpha = 0^\circ$ and 45° Type II. Such an edge effect is attributed to the lack of loading symmetry, which resulted in a z (through-thickness) direction force at these end nodes. The relative densities (calculated using Eq. (1)), t/l ratios,

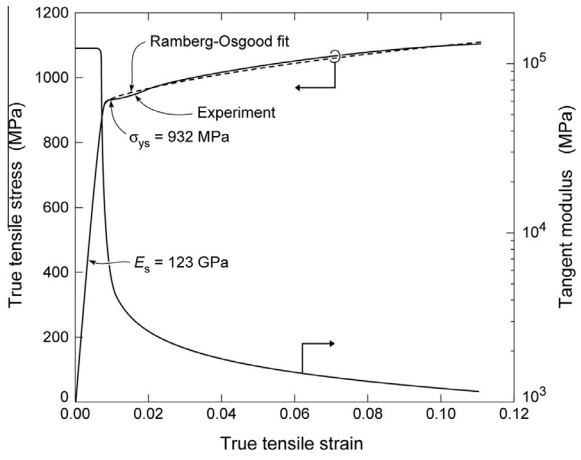

Fig. 9. True tensile stress–strain response of the Ti–6Al–4V alloy after exposure to the thermal cycle used for brazing. A modified Ramberg–Osgood fit to the stress–strain response is also shown. The tangent modulus as a function of strain (obtained as the derivative of the modified Ramberg–Osgood curve) is also overlaid on the data.

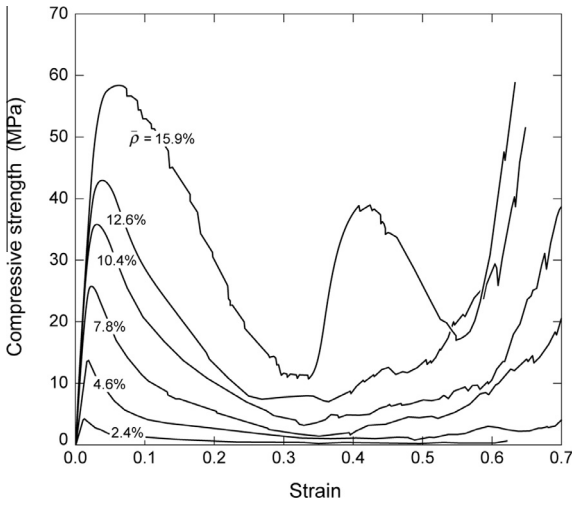

Fig. 10. Compressive stress–strain responses of snap-fit Ti–6Al–4V octet-truss lattice samples with different relative densities.

elastic shear moduli and shear strengths of shear samples are summarized in Tables 3–5.

4. DFA and generalized models for octet-truss lattice

The mechanical properties of the ideal octet-truss lattice material (attained in the limit of vanishing node volume) have been analyzed by Deshpande et al. (2001). This DFA model examined an ideal octahedral cell, and the results apply to the octet-truss lattice constructed by a 3-D stacking of such octahedral unit cells. It was shown that for small t/l, the contribution to overall stiffness of the octet-truss lattice from the bending of the struts was negligible compared to that from strut stretching. The DFA model assumed pin-joined struts, and applied a first order approximation to the relative density with the form $\bar{\rho}_{\text{oct}} = 6\sqrt{2}\left(\frac{t}{l}\right)^2$ (Eq. (3)) which slightly overestimates the relative density due to a double counting of the small nodal volume. The DFA model assumed the octahedral cell had a "face-centered-cubic" symmetry; there are three independent elastic compliance constants, S_{ij} (the contracted indices i and j are ordered pairs of Cartesian indices) for a cubic system, i.e., the set $\{S_{xxxx}, S_{xxyy}, S_{yzyz}\}$ (equivalent to $\{S_{11}, S_{12}, S_{44}\}$ with contracted indices), and the linear elastic strain, ε_i and stress, σ_j tensor relationship took the form (with Cartesian indices);

$$\begin{bmatrix} \varepsilon_{xx} \\ \varepsilon_{yy} \\ \varepsilon_{zz} \\ \varepsilon_{yz} \\ \varepsilon_{xz} \\ \varepsilon_{xy} \end{bmatrix} = \begin{bmatrix} S_{xxxx} & S_{xxyy} & S_{xxyy} & 0 & 0 & 0 \\ S_{xxyy} & S_{xxxx} & S_{xxyy} & 0 & 0 & 0 \\ S_{xxyy} & S_{xxyy} & S_{xxxx} & 0 & 0 & 0 \\ 0 & 0 & 0 & S_{yzyz} & 0 & 0 \\ 0 & 0 & 0 & 0 & S_{yzyz} & 0 \\ 0 & 0 & 0 & 0 & 0 & S_{yzyz} \end{bmatrix} \begin{bmatrix} \sigma_{xx} \\ \sigma_{yy} \\ \sigma_{zz} \\ \sigma_{yz} \\ \sigma_{xz} \\ \sigma_{xy} \end{bmatrix} \tag{4a}$$

where the components of elastic compliance matrix are given by;

$$\begin{bmatrix} S_{xxxx} & S_{xxyy} & S_{xxyy} & 0 & 0 & 0 \\ S_{xxyy} & S_{xxxx} & S_{xxyy} & 0 & 0 & 0 \\ S_{xxyy} & S_{xxyy} & S_{xxxx} & 0 & 0 & 0 \\ 0 & 0 & 0 & S_{yzyz} & 0 & 0 \\ 0 & 0 & 0 & 0 & S_{yzyz} & 0 \\ 0 & 0 & 0 & 0 & 0 & S_{yzyz} \end{bmatrix} = \frac{1}{\bar{\rho}_{\text{oct}} E_s} \begin{bmatrix} 9 & -3 & -3 & 0 & 0 & 0 \\ -3 & 9 & -3 & 0 & 0 & 0 \\ -3 & -3 & 9 & 0 & 0 & 0 \\ 0 & 0 & 0 & 12 & 0 & 0 \\ 0 & 0 & 0 & 0 & 12 & 0 \\ 0 & 0 & 0 & 0 & 0 & 12 \end{bmatrix} \tag{4b}$$

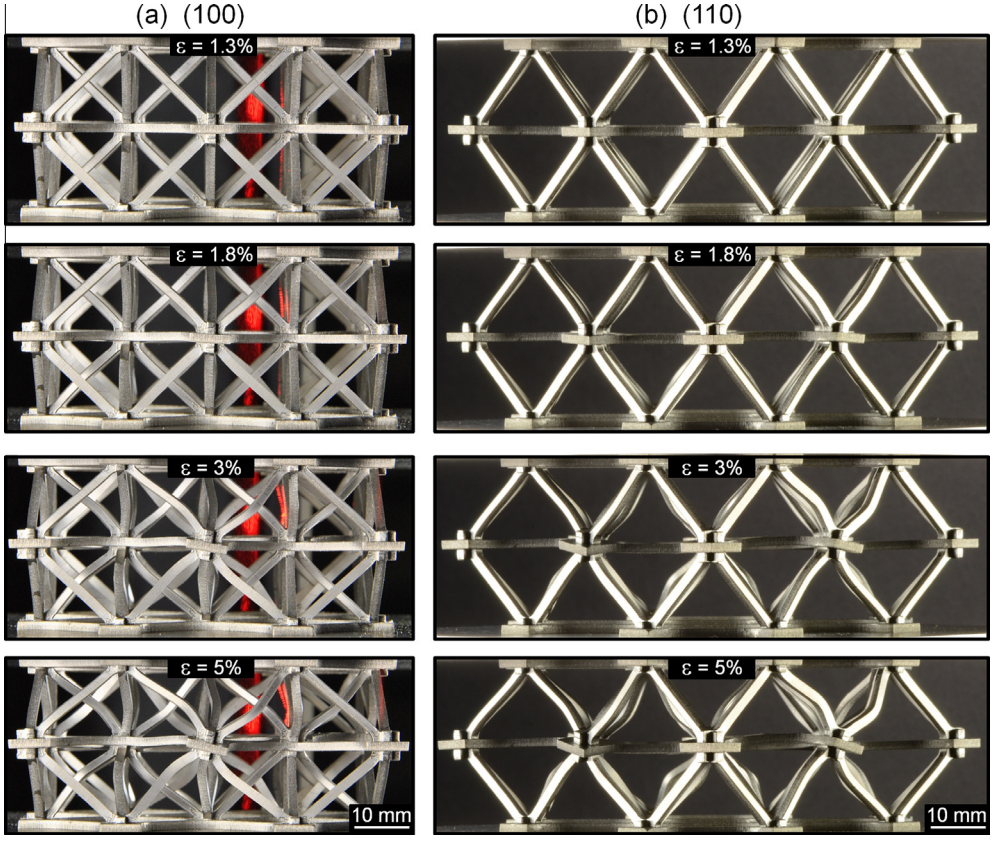

Fig. 11. Photographs of (a) the (1 0 0) and (b) the (1 1 0) planes of a lattice with $\bar{\rho} = 4.6\%$ during compression. The development of inelastic truss buckling can be seen as the total strain, ε, increased.

Table 2
Relative densities, t/l ratio, experimental and unit cell compressive moduli and strengths of the manufactured snap-fit Ti–6Al–4V octet-truss lattice compression specimens. The relative densities were calculated using Eq. (1).

Strut length (l, mm)	t/l	Relative density ($\bar{\rho}$) (%)	Sample compressive stiffness (GPa)	Unit cell compressive stiffness (GPa)	Sample compressive strength (MPa)	Unit cell compressive strength (MPa)	Energy absorption per unit volume, W_v (MPa)
25.400	0.063	2.4	0.49	0.39	4.2	3.5	0.52
16.891	0.094	4.6	0.97	0.78	14.1	11.9	2.99
12.014	0.132	7.8	2.04	1.64	26.3	22.5	6.11
9.728	0.163	10.4	2.69	2.16	35.7	30.8	9.52
8.433	0.188	12.6	3.49	2.81	44.2	38.4	12.24
7.010	0.226	15.9	4.94	3.98	56.5	49.4	21.16

where E_s refers to the Young's modulus of the strut material. The principal material axes, as shown in Fig. 4(c), are defined as a Cartesian co-ordinate system for the analysis.

4.1. Stiffness predictions

The DFA model (Deshpande et al., 2001) predicts the z ([001] through-thickness) direction Young's modulus;

$$E_{zz} = \Sigma_{el}^{E}\bar{\rho}_{\text{oct}}E_s = \frac{1}{9}\bar{\rho}_{\text{oct}}E_s \tag{5}$$

where Σ_{el}^{E} is the elastic compressive modulus coefficient with a value of 1/9, $\bar{\rho}_{\text{oct}}$ is the relative density given by Eq. (3), and E_s is the Young's modulus of the solid material from which the lattice was constructed. The relative compressive modulus, $\frac{E_{zz}}{E_s} = \frac{2\sqrt{2}}{3}\left(\frac{t}{l}\right)^2$, is linearly related to the elastic compressive modulus coefficient and the ideal octet relative density, $\bar{\rho}_{\text{oct}}$.

The (001) in-plane shear modulus is given by;

$$G_{zx} = \Sigma_{el}^{G}\bar{\rho}_{\text{oct}}E_s = \frac{1}{12}\bar{\rho}_{\text{oct}}E_s \tag{6}$$

where Σ_{el}^{G} is an elastic shear modulus coefficient with a value of 1/12, and the relative (001) in-plane shear modulus is $\frac{G_{zx}}{E_s} = \frac{\sqrt{2}}{2}\left(\frac{t}{l}\right)^2$. The relative shear modulus, $\frac{G_{zx}}{E_s}$ is therefore linearly related to the elastic shear modulus coefficient, Σ_{el}^{G}, and the ideal octet relative density, $\bar{\rho}_{\text{oct}}$. The cubic symmetry dictates that the (001) in-plane shear modulus is independent of the shear direction in this plane.

The DFA model predicts density independent (constant) elastic stiffness coefficients $\left(\Sigma_{el}^{E} \text{ and } \Sigma_{el}^{G}\right)$; a consequence the DFA models analysis of an ideal octahedral cell without the nodal volume of real samples taken into account. This can be addressed using the free body diagram method (Finnegan et al., 2007), which shows that the total external force required for each individual strut to achieve an identical state of strain is a constant. As shown in Appendix B, the elastic modulus coefficient, Σ_{el}, is linearly related to the specimens octahedral cell height (H), its cross-section area (A), and the relative density $\bar{\rho}$ now given by Eq. (1);

$$\Sigma_{el} = K_{el}\frac{H}{lA\bar{\rho}} \tag{7a}$$

The relative compressive modulus is then given by;

$$\frac{E_{zz}}{E_s} = \Sigma_{el}^{E}\bar{\rho} = K_{el}^{E}\frac{H}{lA} \tag{7b}$$

The relative (001) in-plane shear modulus is given by;

$$\frac{G}{E_s} = \Sigma_{el}^{G}\bar{\rho} = K_{el}^{G}\frac{H}{lA} \tag{7c}$$

where K_{el} is a constant with $K_{el}^{E} = \frac{2}{3}t^2$ for the compressive modulus coefficient, and $K_{el}^{G} = \frac{1}{2}t^2$ for the (001) in-plane shear modulus coefficient. The specimen octahedral cell height (H), its cross-sectional area (A) and the relative density ($\bar{\rho}$) are all now functions of the nodal geometry of the lattices tested here.

In the limiting DFA model case, $H = \sqrt{2}l$, and $A = l^2$, and the compressive modulus coefficient, relative compressive modulus, shear modulus coefficient, and relative shear modulus given by Eq. (7) reduce to $\frac{1}{9}$, $\frac{2\sqrt{2}}{3}\left(\frac{t}{l}\right)^2$, $\frac{1}{12}$, and $\frac{\sqrt{2}}{2}\left(\frac{t}{l}\right)^2$ respectively (i.e. the DFA model predictions). Eq. (7) is subsequently referred to as a generalized octet-truss lattice elastic modulus model which can be used to analyze the snap-fit octet-truss lattice whose struts do not make contact at a node (non-zero values of b, c, h, h_{tab}, m, in Fig. 4) and therefore contains extra nodal mass.

4.2. Strength predictions

4.2.1. Compressive strength

A stretch dominated cellular lattice may collapse under compressive loading by elastic or inelastic buckling, or by plastic yielding depending on the slenderness (t/l ratio for a solid strut of length l and square cross section of side length t) of the struts.

At high relative densities, l tends towards t, and a lattice will fail by yielding of the low aspect ratio struts. Lattice strength, σ_{pk} then linearly scales with the yield strength, σ_{ys} of the solid material, and the load bearing area (i.e. relative density, $\bar{\rho}$) of the lattice;

$$\sigma_{pk} = \sigma_{ys}\bar{\rho}\Sigma_{\sigma} \tag{8}$$

where Σ_{σ} is a lattice topology (strut orientation) dependent strength coefficient (Wadley, 2006).

At low densities, struts are slender enough to collapse by elastic buckling prior to compressive plastic yielding, and lattice strength is obtained by replacing the strut material yield strength, σ_{ys} in Eq. (8), with the elastic buckling stress given by;

$$\sigma_{\text{E}} = \frac{k^2\pi^2E_sI}{Al^2} = \frac{k^2\pi^2E_s}{12}\left(\frac{t}{l}\right)^2 \tag{9}$$

where I is the second moment of area of the strut, A is the strut cross-sectional area ($I = \frac{t^4}{12}$, $A = t^2$, for a solid strut with square cross section of side length t) and the factor k is determined by the end conditions on the buckling struts. If the ends of the struts are pin-jointed, and can freely rotate $k = 1$ while selection of $k = 2$ corresponds to a strut whose ends are buried and cannot rotate during buckling.

At intermediate relative densities, buckling occurs after the stress in the strut has exceeded the proportional limit of the solid material, but before the stress attains the ultimate strength of the solid. In this case, the compressive strength of the lattice is controlled by inelastic buckling at an inelastic bifurcation stress given by the tangent modulus theory (Gere and Timoshenko, 1984; Shanley, 1967). In this case the compressive strength is found by replacing E_s in Eq. (9) by the tangent modulus E_t at an inelastic bifurcation stress level, i.e., by replacing σ_{E} with σ_{IE} given by:

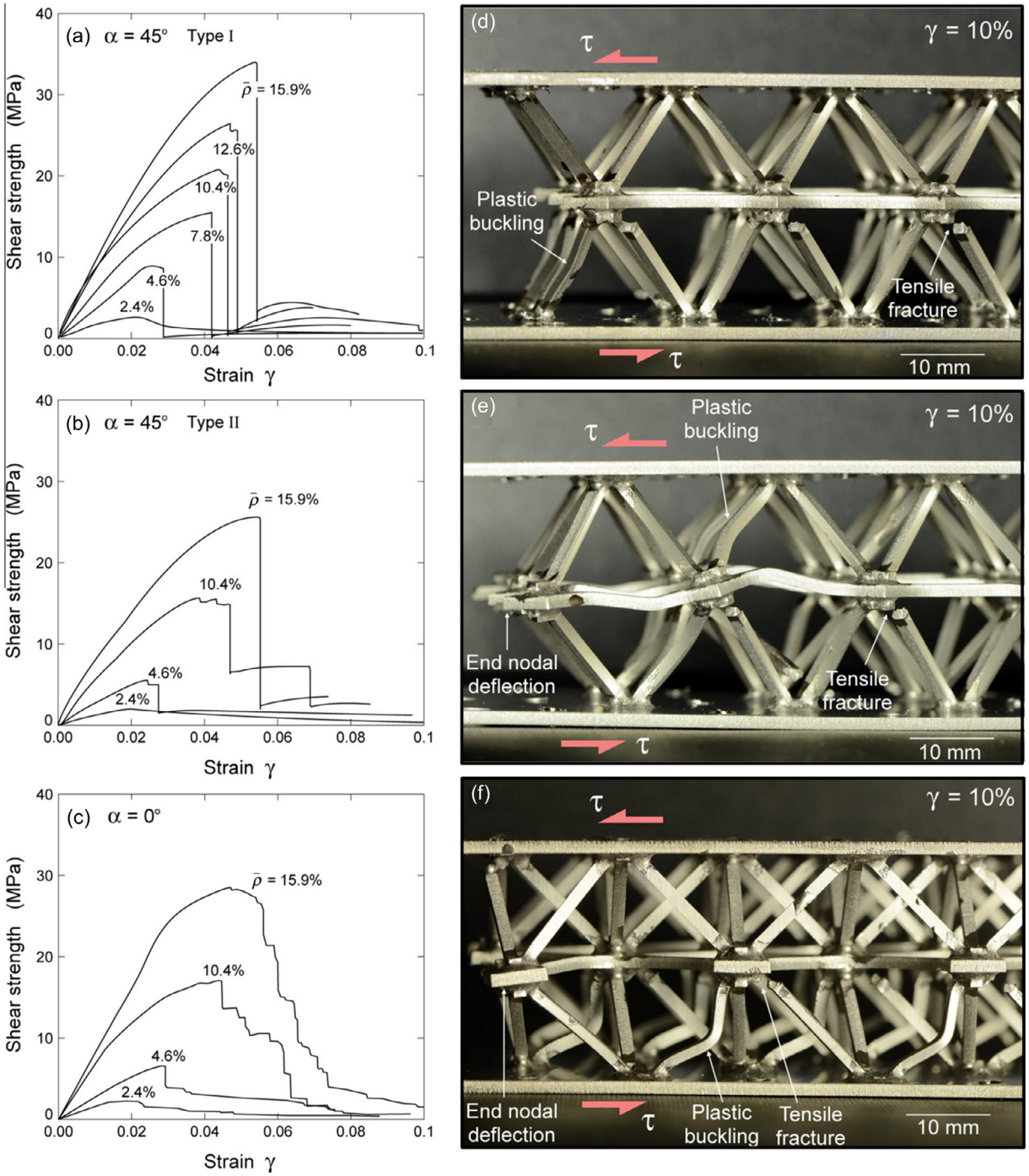

Fig. 12. Shear stress–strain responses for (a) Type I and (b) Type II Ti–6Al–4V octet-truss lattice shear specimens of different relative densities loaded in the $\alpha = 45°$ direction. Lattice responses when loaded in the $\alpha = 0°$ direction are shown in (c). Photographs revealing the failure modes are also shown for Type I (d) Type II (e) and $\alpha = 0°$ (f) shear samples all with $\bar{\rho} = 4.6\%$.

$$\sigma_{IE} = \frac{k^2\pi^2 E_t I}{Al^2} = \frac{k^2\pi^2 E_t}{12}\left(\frac{t}{l}\right)^2 \tag{10}$$

The DFA model for the ideal octet-truss lattice assumed the strut material to be elastic-perfectly plastic with a tangent modulus of zero; therefore the only mechanisms for lattice failure were elastic buckling and plastic yielding. In the case of an ideal octet-truss lattice with a vanishing node size, and with the principal axes defined as shown in Fig. 4(c), the DFA model Deshpande et al., 2001 predicts the z (or [0 0 1]) direction compressive strength when the elastic buckling failure mechanism is operative;

$$\sigma_{zz}^{pk} = \frac{\pi^2 E_s}{36}\bar{\rho}_{oct}\left(\frac{t}{l}\right)^2 \tag{11}$$

The DFA model assumes $k = 1$ for the end conditions of the struts, though the precise value is likely to be influenced by the node design and the mechanical properties of the solid material used to make the structure.

In the case of plastic yielding governed failure;

$$\sigma_{zz}^{pk} = \frac{1}{3}\bar{\rho}_{oct}\sigma_{ys} \tag{12}$$

Table 3
Relative densities, t/l ratio, experimental and unit cell shear moduli and strengths of the manufactured snap-fit Ti–6Al–4V octet-truss lattice shear specimens ($\alpha = 0°$). The relative densities were calculated using Eq. (1).

Strut length (l, mm)	t/l	Relative density ($\bar{\rho}$) (%)	Sample shear stiffness (GPa)	Unit cell shear stiffness (GPa)	Sample shear strength (MPa)	Unit cell shear strength (MPa)
25.400	0.063	2.4	0.35	0.28	2.3	1.9
16.891	0.094	4.6	0.69	0.55	6.7	5.6
12.014	0.132	7.8	–	–	–	–
9.728	0.163	10.4	1.88	1.48	16.9	14.3
8.433	0.188	12.6	–	–	–	–
7.010	0.226	15.9	3.60	2.84	28.5	24.4

For a material with a non-zero tangent modulus, the inelastic buckling criterion can be simply obtained by replacing E_s in Eq. (11) with E_t, to give;

$$\sigma_{zz}^{pk} = \frac{\pi^2 E_t}{36}\bar{\rho}_{oct}\left(\frac{t}{l}\right)^2 \tag{13}$$

In Eqs. (11)–(13), $\bar{\rho}_{oct}$ refers to that given by Eq. (3).

The snap-fit octet-truss lattice structures fabricated here have a considerable node volume and struts ends are laterally separated which requires the nodal geometry to be explicitly addressed. Since the total external force required for each individual strut to achieve an identical state of strain is a constant, a more general expression for the compressive strength coefficient (Σ_σ), assuming pin-joined struts ($k = 1$), as a function of the specimen octahedral cell cross-sectional area, A and relative density, $\bar{\rho}$ was derived in Appendix B;

$$\Sigma_\sigma = K_\sigma \frac{\sigma_c}{A\bar{\rho}} \tag{14a}$$

and the relative compressive strength is defined as

$$\frac{\sigma_{zz}^{pk}}{\sigma_{ys}} = \Sigma_\sigma \bar{\rho} = K_\sigma \frac{\sigma_c}{A} \tag{14b}$$

where K_σ is a constant $= \frac{2\sqrt{2}t^2}{\sigma_{ys}}$ and σ_c refers to the collapse strength of a single strut, given by σ_{ys} in the case of the plastic yielding failure mode or the critical buckling stresses given by Eqs. (9) and (10) for the corresponding buckling failure modes, and $\bar{\rho}$ in Eq. (14) is that defined in Eq. (1). It can be shown that in the limit of vanishing nodal volume, Eq. (14) reduces to the DFA model prediction (Eqs. (11)–(13)).

4.2.2. The (0 0 1) in-plane shear strength

The (001) in-plane shear strength depends on the shear loading direction in the plane. For $\alpha = 0°$, the measured shear strength $\tau_{0°}^{pk}$ is τ_{zx}^{pk}, with the principal axes defined as shown in Fig. 4(c). The DFA model for an ideal octet-truss lattice with vanishing node volume predicts (Deshpande et al., 2001) that failure by elastic buckling results in a lattice shear strength given by;

$$\tau_{0°}^{pk} = \tau_{zx}^{pk} = \frac{\pi^2 E_s}{72}\bar{\rho}_{oct}\left(\frac{t}{l}\right)^2 \tag{15}$$

For failure by plastic yielding;

$$\tau_{0°}^{pk} = \tau_{zx}^{pk} = \frac{1}{6}\bar{\rho}_{oct}\sigma_{ys} \tag{16}$$

When failure occurs by inelastic buckling;

$$\tau_{0°}^{pk} = \tau_{zx}^{pk} = \frac{\pi^2 E_t}{72}\bar{\rho}_{oct}\left(\frac{t}{l}\right)^2 \tag{17}$$

In Eqs. (15)–(17) $\bar{\rho}_{oct}$ is that defined in Eq. (3).

In the case of $\alpha = 45°$, the measured shear strength, $\tau_{45°}^{pk}$, of the ideal octet-truss lattice when failure occurs by elastic buckling is given by;

$$\tau_{45°}^{pk} = \frac{\sqrt{2}\pi^2 E_s}{72}\bar{\rho}_{oct}\left(\frac{t}{l}\right)^2 \tag{18}$$

When failure occurs by plastic yield, the shear strength is;

$$\tau_{45°}^{pk} = \frac{\sqrt{2}}{6}\bar{\rho}_{oct}\sigma_{ys} \tag{19}$$

While for inelastic buckling, the shear strength is given by;

$$\tau_{45°}^{pk} = \frac{\sqrt{2}\pi^2 E_t}{72}\bar{\rho}_{oct}\left(\frac{t}{l}\right)^2 \tag{20}$$

Eqs. (18)–(20) are DFA model predictions, and $\bar{\rho}_{oct}$ therefore refers to that given by Eq. (3).

A more general expression for the (001) in-plane shear strength coefficient (Σ_τ) of the snap-fit octet-truss lattice can be written as a function of the specimen cross-sectional area, A and relative density, $\bar{\rho}$ (see Appendix B);

$$\Sigma_\tau = K_\tau \frac{\sigma_c}{A\bar{\rho}} \tag{21a}$$

While the relative (001) in-plane shear strength is;

$$\frac{\tau}{\sigma_{ys}} = \Sigma_\tau \bar{\rho} = K_\tau \frac{\sigma_c}{A} \tag{21b}$$

where K_τ is a constant. For $\alpha = 0°$, $K_\tau = \frac{\sqrt{2}t^2}{\sigma_{ys}}$ while for $\alpha = 45°$, $K_\tau = \frac{2t^2}{\sigma_{ys}}$, if it is assumed that the struts are pin-joined. In Eq. (21), $\bar{\rho}$ now refers to that given by Eq. (1).

5. Comparison of predictions with measurements

Before comparisons between the measured and modeled properties of the snap-fit lattice can be made, it is necessary to adjust the measured properties of the compression, Fig. 5(c) and $\alpha = 0°$ shear samples, Fig. 6(c), to account for edge struts that belong to

Table 4
Relative densities, t/l ratio, experimental shear moduli and strengths of the manufactured snap-fit Ti–6Al–4V octet-truss lattice shear specimens ($\alpha = 45°$, Type I). The relative densities were calculated using Eq. (1).

Strut length (l, mm)	t/l	Relative density ($\bar{\rho}$) (%)	Shear stiffness (GPa)	Shear strength (MPa)
25.400	0.063	2.4	0.31	2.6
16.891	0.094	4.6	0.61	8.5
12.014	0.132	7.8	1.14	15.7
9.728	0.163	10.4	1.76	21.0
8.433	0.188	12.6	2.33	26.7
7.010	0.226	15.9	2.56	34.4

Table 5
Relative densities, t/l ratio, experimental shear moduli and strengths of the manufactured snap-fit Ti–6Al–4V octet-truss lattice shear specimens ($\alpha = 45°$, Type II). The relative densities were calculated using Eq. (1).

Strut length (l, mm)	t/l	Relative density ($\bar{\rho}$) (%)	Shear stiffness (GPa)	Shear strength (MPa)
25.400	0.063	2.4	0.22	2.0
16.891	0.094	4.6	0.41	6.2
12.014	0.132	7.8	–	–
9.728	0.163	10.4	1.07	15.6
8.433	0.188	12.6	–	–
7.010	0.226	15.9	1.89	25.6

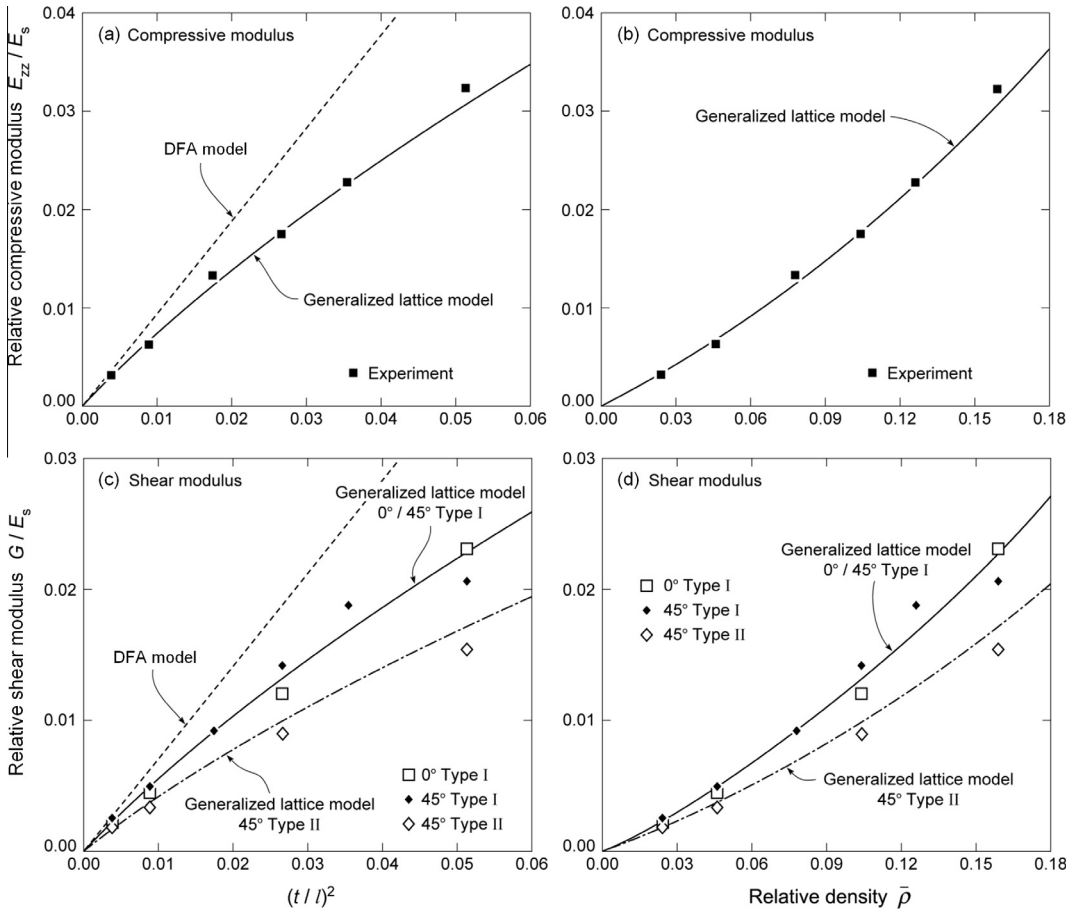

Fig. 13. Comparisons between the measured and model predicted relative elastic moduli (normalized by solid material modulus) as a function of $(t/l)^2$ and relative density $\bar{\rho}$ for the snap-fit lattice. The corresponding predictions of the DFA model (which assumes a vanishing node volume) and the generalized octet-truss lattice model (which accounts for the nodal separation and additional nodal mass of the snap-fit structure) are shown in (a) and (c) as a function of the strut aspect ratio. "Generalized lattice model" is the abbreviation of "generalized octet-truss lattice model".

the unit cells of a larger area sample. These edge struts of partial unit cells contribute both stiffness and strength to the samples mechanical response. If it is assumed the edge struts of adjacent cells behave in the same manner as their inner strut counterparts, the total force required to deform the counterpart lattice without redundant edge struts can be shown (by taking the ratio of the number of out-of-plane struts that contribute stiffness/strength in lattices without extra edge struts to the total number of out-of-plane struts in the tested samples. All the out-of-plane struts contribute stiffness/strength for compression samples, whereas only the 0° orientated out-of-plane struts are taken into account for the $\alpha = 0^\circ$ shear samples) to be 4/5 that of the snap-fit lattice samples actually tested. The strength of a lattice without extra edge struts is then given by this applied force divided by its cross-sectional area, and is subsequently defined as the unit cell strength; the unit cell stiffness is then obtained as this stress divided by the imposed strain. It is noted here that the manufactured samples have a height of $H + t$; whereas, the octahedral cell as shown in Fig. 4(c) has a height of H. Tables 2 and 3 summarize the sample and unit cell moduli and strengths of both the compression and $\alpha = 0^\circ$ shear lattice samples. Since there are no redundant out-of-plane edge struts in the $\alpha = 45^\circ$ shear lattice samples tested here; the definition of "unit cell stiffness/strength" was not used in the $\alpha = 45^\circ$ case.

The mechanical properties of a lattice reviewed in Section 4, are a function of its number and orientation of struts and the strut t/l ratio, as well as strut material mechanical properties. The nodes are parasitic mass which do not change the strut response, as long as k, the factor accounting for the rotational stiffness of the truss ends, is not affected. The unit cell elastic moduli for compression and $\alpha = 0^\circ$ shear samples are therefore plotted against $\left(\frac{t}{l}\right)^2$, in Fig. 13(a) and (c), and the relative compressive and shear strengths against $\left(\frac{t}{l}\right)^2$ in Figs. 14(a) and 15(a) and (c) since this abscissa scales with the relative density of both an ideal octet-truss lattice and the snap-fit structure. The DFA model predictions are overlaid on these results. The elastic moduli are also plotted against the snap-fit structures relative density, $\bar{\rho}$, which includes the parasitic nodal mass (as given by Eq. (1)), in Fig. 13(b) and (d), and the strength data in Figs. 14(b) and 15(b) and (d). Generalized octet-truss lattice model predictions are plotted against both $\left(\frac{t}{l}\right)^2$ and the snap-fit structures relative density, $\bar{\rho}$, which takes into account the extra nodal volume, on all the figures.

The relative elastic moduli (E_{zz}/E_s and G/E_s) for the snap-fit Ti–6Al–4V octet-truss lattice structure deduced from the measured unit cell relative elastic moduli for compression and $\alpha = 0^\circ$ shear samples are shown in Fig. 13 as a function of $\left(\frac{t}{l}\right)^2$ and the snap-fit structures relative density $\bar{\rho}$. Examination of Fig. 13(a) and (b) shows that the compressive modulus data is over predicted by the DFA model but is in excellent agreement with the generalized octet-truss lattice model which accounts for actual nodal geometry of the tested samples. Fig. 13(c) and (d) show three sets of experimental data for the relative shear moduli measured at $\alpha = 0^\circ$, and for both the Type I and II shear structures tested at

$\alpha = 45°$. It is evident that the DFA model is unable to predict the snap-fit structures responses; a consequence of the strut separation at the nodes. By taking into account the nodal geometry, the generalized octet-truss lattice model predictions agree well with the $\alpha = 45°$ Type I and $\alpha = 0°$ measurements. However, the generalized shear modulus model is still unable to predict the $\alpha = 45°$ Type II structure response as well. In the DFA model, nodal rotations during shear loading were constrained by symmetry during the analysis. In the $\alpha = 45°$ Type II case experiments, insufficient nodal connectivity at the end nodes of the finite length samples led to substantial nodal rotation, Fig. 12(e). The edge struts connecting these end nodes then made a reduced (negligible) contribution to the core stiffness since they underwent little axial (stretching) deformation. If the stiffness contribution from the edge struts connecting the end nodes (a quarter of the struts) is neglected, the shear stiffness of the as manufactured $\alpha = 45°$ Type II core would be approximately 3/4 (by taking the ratio of the number of out-of-plane struts that contribute stiffness to the total number of out-of-plane struts in the tested $\alpha = 45°$ Type II shear samples) that of $\alpha = 45°$ Type I core. The generalized octet-truss lattice shear stiffness model prediction for the $\alpha = 45°$ has been multiplied by 3/4, and is shown to then be in good agreement with the $\alpha = 45°$ Type II measurement when plotted against $\left(\frac{t}{l}\right)^2$ in Fig. 13(c) or the snap-fit structures relative density in Fig. 13(d).

The relative unit cell compressive strength as a function of the snap-fit structures $\left(\frac{t}{l}\right)^2$ ratio and relative density are shown in Fig. 14(a) and (b). The unit cell data is compared with both the DFA model and generalized octet-truss lattice model predictions. The trend in the experimental data changed abruptly at $\bar{\rho} = 0.046$ as the failure mechanism changes from elastic to inelastic buckling of the out-of-plane struts. The measurements are in good agreement with the generalized octet-truss lattice models for these two mechanisms: at low relative density ($\bar{\rho} < 0.046$), the measurements follow the elastic buckling model. The measurements then become consistent with the inelastic buckling model when $\bar{\rho} > 0.046$. Since the Ti–6Al–4V alloy exhibits low strain hardening, the inelastic buckling model converges rapidly with the plastic yielding model when $\bar{\rho} > 0.10$. The generalized octet-truss lattice model slightly underestimated the compressive strength for $\bar{\rho} > 0.13$; consistent with increased node rotation resistance for high t/l ratios. The generalized octet-truss lattice model assumed pin-joined struts at these nodes, ($k = 1$). However the nodes of the stubby struts appear to have a rotational stiffness k that lies between 1 and 2 for the octet-truss lattice structures made here.

Fig. 15 shows the relative (001) in-plane shear strength of the shear samples versus their relative density and compares them with both the DFA model and the generalized octet-truss lattice model predictions for (a) $\alpha = 45°$ (001) in-plane shear and (b) α $\alpha = 0°$ (001) in-plane shear. Like the compressive responses, the experimental data changed abruptly at $\bar{\rho} = 0.046$, which is consistent with a change of failure mode from elastic to inelastic buckling. Again, the DFA model is not able to predict the shear strengths of the snap-fit lattices. The generalized octet-truss lattice model is able to predict the shear strength of the $\alpha = 0°$ and Type I $\alpha = 45°$ samples: the measurements follow the elastic buckling mode at low relative density ($\bar{\rho} < 0.046$), with a transition to the inelastic buckling mode at $\bar{\rho} \approx 0.046$, and to the plastic yielding mode beyond $\bar{\rho} \approx 0.1$. However, the generalized octet-truss lattice model fails to predict the case of $\alpha = 45°$ Type II. The discrepancies again arise from the sample edge effect as mentioned above: the out-of-plane edge struts connecting the end nodes suffer minimal axial deformations, and thus make a negligible contribution to the in-plane shear strength of the core. Since the fraction of out-of-plane struts that do not suffer an edge effect is 3/4 of the total pyramidal struts, we estimate that the in-plane shear strength of the $\alpha = 45°$ Type II cores should be approximately 3/4 that of $\alpha = 45°$ Type I cores; the measurements are consistent with this prediction by multiplying 3/4 to the generalized octet-truss lattice model shear strength prediction for $\alpha = 45°$ Type I cores (Fig. 15(c)). Comparison of model results and measurements indicates that for low aspect ratio octet-truss lattice structures, the in-plane shear strength is sensitive to boundary conditions when the edge nodes have insufficient nodal connectivity to induce strut stretching.

6. Comparisons with competing materials

The measured compressive moduli and strengths of the snap-fit Ti–6Al–4V octet-truss lattices investigated here were included in the material property charts of Fig. 2. These two maps do not show the properties of other anisotropic topology cellular structures, which excel in performance under some loading conditions but are inferior in others. The properties of the titanium octet-truss lattice are clearly superior to the lattice structures made from investment cast Al–7Si–0.3Mg (Deshpande et al., 2001), Ti–6Al–4V, and Ti–6Al–2Sn–4Zr–2Mo alloys (Li et al., 2008a,b), as well as Ni–7P deposited via electrodeposition (Torrents et al., 2012), lattices made from carbon fiber laminate composites (Cheung and Gershenfeld, 2013), photosensitive HDDA polymers and vapor deposited alumina (with solid trusses) (Zheng et al., 2014), and are very competitive with the Al_2O_3-polymer hybrid octet-truss lattices (Bauer et al., 2014).

The Ti–6Al–4V octet-truss lattices investigated here are more robust than brittle Al_2O_3 counterparts, and are expected to retain good dimensional stability during loading at temperature up to approximately 400 °C. However, a solid truss has a lower second area moment than a hollow truss and thus a lower resistance to elastic buckling; the strengths of the titanium octet-truss lattices with solid trusses loaded in compression are therefore inferior to the electrodeposited hollow truss alumina and Ni–7P octet-truss lattices (Zheng et al., 2014) for densities lower than 0.18 Mg/m^3 where the elastic buckling failure mechanism of the solid struts is dominant (solid model prediction line shown in Fig. 2(b)). However, it is evident that the predicted compressive moduli of the titanium octet-truss lattices are superior to the hollow truss Ni–7P octet-truss lattices (Zheng et al., 2014) and very competitive with the hollow truss alumina octet-truss lattices (Zheng et al., 2014) at the lower density range (<0.18 Mg/m^3).

The shear moduli and strengths of the Ti–6Al–4V octet-truss lattices are compared with those of metal and polymer foams and several engineering alloys and carbon fiber reinforced polymers (CFRP) in Fig. 16. They are significantly superior to foamed structures and may therefore provide interesting opportunities for high temperature sandwich panel and thermal management applications.

7. Conclusions

1. Ti–6Al–4V octet-truss lattice structures with relative densities in the range 2–16% have been manufactured via a snap-fit and vacuum brazing approach.
2. The lattice structures elastic stiffness constants and strengths have been measured under through-thickness free compression and in-plane shear loading as a function of $\left(\frac{t}{l}\right)^2$ and the snap-fit structures relative density. The failure mechanism changes from elastic buckling to inelastic buckling at a relative density of about 0.05.

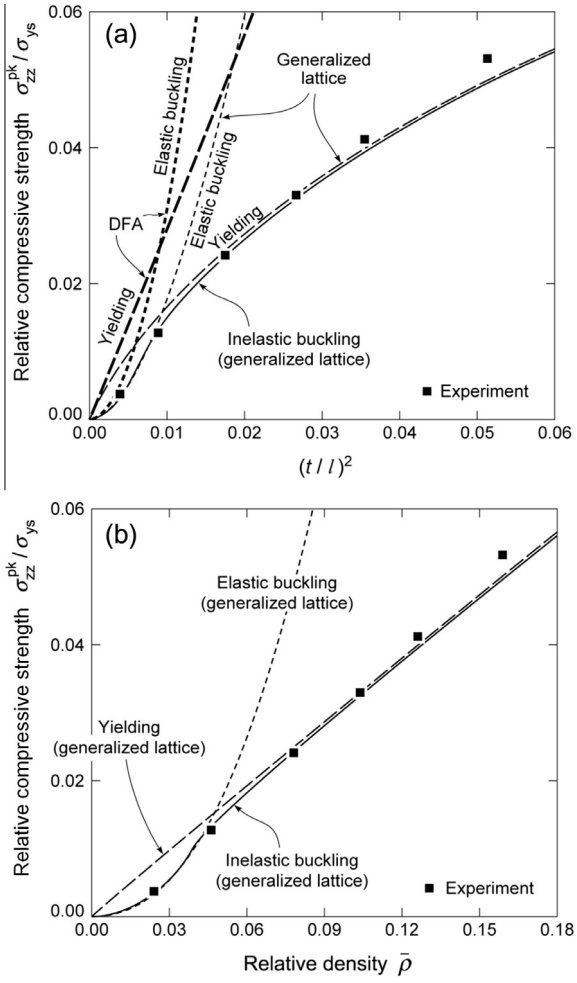

Fig. 14. Predicted and measured relative compressive strength (normalized by the solids yield strength) plotted against (a) $(t/l)^2$ and (b) relative density $\bar{\rho}$ of the snap-fit structure. Both the DFA model and generalized octet-truss lattice model predictions are shown in (a) as a function of strut aspect ratio. "Generalized lattice model" is the abbreviation of "generalized octet-truss lattice model".

3. The moduli and strengths of the manufactured octet-truss lattice structures are well predicted by a generalized octet-truss lattice model. However, the (001) in-plane shear moduli and strengths are sensitive to boundary conditions for small aspect ratio octet-truss lattice structures.
4. The Ti–6Al–4V octet-truss lattices exhibit excellent overall mechanical properties competitive with existing materials and topologies, and appear to be a promising candidate for high temperature, sandwich panel and other applications.

Acknowledgments

We are grateful for the support of this work by the DARPA MCMA program (Grant Number W91CRB-10-1-005) managed by Dr. Judah Goldwasser.

Appendix A. Modified Ramberg–Osgood fitting

The true tensile stress–strain curve was separated into two parts and fitted separately.

For $\sigma < \sigma_{0.2}$, $n = 85$, $E_0 = 123$ GPa, $\sigma_{0.2} = 932$ MPa, Ramberg–Osgood fitting

$$\varepsilon = \frac{\sigma}{E_0} + 0.002\left(\frac{\sigma}{\sigma_{0.2}}\right)^n$$

For $\sigma > \sigma_{0.2}$, a modified Ramberg–Osgood fitting (Rasmussen, 2003) was applied by moving both vertical and horizontal axes from the origin to a selected point which enabled a smooth transition between the two fitting curves. This new origin had coordinates $\varepsilon_1 = 0.0085$, $\sigma_1 = 925$ MPa, with an initial Young's modulus $E_1 = 9.77$ GPa, The fitting coefficients for the modified Ramberg–Osgood relation were then $n = 1.7$, $\varepsilon_u = 0.1105$, $\sigma_u = 1110$ MPa, with

$$\varepsilon - \varepsilon_1 = \frac{\sigma - \sigma_1}{E_1} + \left(\varepsilon_u - \varepsilon_1 - \frac{\sigma_u - \sigma_1}{E_1}\right)\left(\frac{\sigma - \sigma_1}{\sigma_u - \sigma_1}\right)^n$$

Appendix B. Generalized octet-truss lattice model

B.1. Compression

B.1.1. Compressive modulus

Consider an edge clamped out-of-plane strut of the octahedral cell with length l and square cross section of side length t as shown in Fig. A1(a). During free compression, both ends of an out-of-plane strut are able to move due to the Poisson effect of the octahedral cell. Fig. A1 illustrates the deformation behavior of an end clamped out-of-plane strut when the octahedral cell is under free compression. The corresponding free body diagram of such a strut is shown in Fig. A1(b). With an imposed displacement at one end along z direction denoted as δ_{zz}, the lateral displacement at the other end along x direction denoted as δ_{xx}, the axial force F_A and shear force F_S in the strut are given by elementary beam theory

$$F_A = E_s t^2 \frac{(\delta_{zz}\sin\omega - \delta_{xx}\cos\omega)}{l} \tag{A-1a}$$

$$F_S = \frac{12E_s I(\delta_{zz}\cos\omega + \delta_{xx}\sin\omega)}{l^3} \tag{A-1b}$$

where E_s is the Young's modulus of the solid material, ω is strut inclined angle (=45°), I is the second moment of area of the strut cross section given by $I = t^4/12$ for square cross section of side length t. The total applied force, F_{strut}, on such a single strut in the z direction follows as

$$F_{strut} = F_A\sin\omega + F_S\cos\omega \tag{A-2a}$$

Eq. (A-2a) applies for fixed-end (built-in) struts ($k = 2$); for pin-joined struts ($k = 1$), the contribution to the stiffness due to the bending of the struts is negligible, and Eq. (A-2a) reduces to

$$F_{strut} = F_A\sin\omega = \frac{E_s t^2(\delta_{zz} - \delta_{xx})}{2l} \tag{A-2b}$$

In the case of pin-joined struts, the basic force analysis showed that the lateral displacement δ_{xx} is related to the vertical displacement δ_{zz} by

$$\delta_{xx} = \frac{1}{3}\delta_{zz} \tag{A-3}$$

Therefore, Eq. (A-2b) reduces to

$$F_{strut} = F_A\sin\omega = \frac{E_s t^2\delta_{zz}}{3l} \tag{A-4}$$

Now consider the octahedral cell sketched in Fig. A1(a). The total force, F, applied on the octahedral cell in the z direction is equal to $4F_{strut}$; stress, σ_{zz} and strain, ε_{zz} applied to the octahedral cell are related to the force F and displacement δ_{zz} via;

$$\sigma_{zz} = \frac{F}{A} = \frac{4E_s t^2\delta_{zz}}{3lA} \tag{A-5}$$

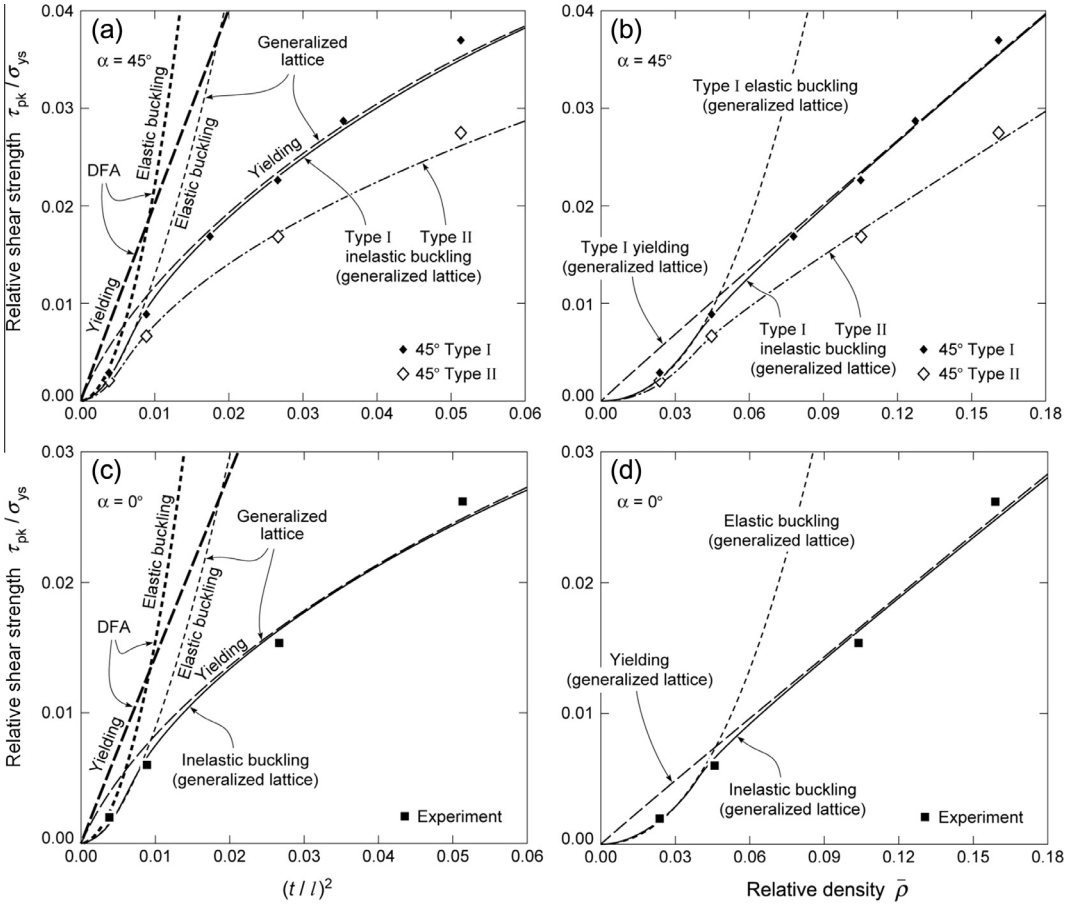

Fig. 15. Predicted and measured relative shear strength for $\alpha = 45°$ plotted against (a) $(t/l)^2$ and (b) relative density $\bar{\rho}$ of the snap-fit structure. Both the DFA model and generalized octet-truss lattice model predictions are shown in (a) and (c). Analogous results for loading at $\alpha = 0°$ are shown in (c) and (d). "Generalized lattice model" is the abbreviation of "generalized octet-truss lattice model".

and

$$\varepsilon_{zz} = \frac{2\delta_{zz}}{H} \tag{A-6}$$

where H is octahedral cell height $H = 2(l\sin\omega + h + 2h_{tab})$, A is cross-sectional area ($A = \left(\frac{2l\cos\omega + b + c}{\sqrt{2}}\right)^2$), as shown in Fig. 4(c). The effective Young's modulus E_{zz} of the octahedral cell in free compression is then given by;

$$E_{zz} = \frac{\sigma_{zz}}{\varepsilon_{zz}} = \frac{2t^2}{3}\frac{H}{lA}E_s \tag{A-7}$$

Eq. (A-7) can be expressed in terms of the relative compressive modulus as

$$\frac{E_{zz}}{E_s} = \frac{2t^2}{3}\frac{H}{lA} = K_{el}\frac{H}{lA} \tag{A-8}$$

with $K_{el} = \frac{2}{3}t^2$.

B.1.2. Compressive strength

Eq. (A-5) gives the compressive stress σ_{zz} applied to the octahedral cell in the z direction; the corresponding axial stress σ_A in an out-of-plane strut is given by

$$\sigma_A = \frac{E_s(\delta_{zz} - \delta_{xx})}{\sqrt{2}l} = \frac{\sqrt{2}E_s\delta_{zz}}{3l} \tag{A-9}$$

Therefore, the stress applied to the octahedral cell, σ_{zz}, can be expressed in terms of the axial stress, σ_A, in an out-of-plane strut;

$$\sigma_{zz} = \frac{2\sqrt{2}t^2}{A}\sigma_A \tag{A-10}$$

The out-of-plane strut can support load until its collapse strength σ_c is achieved. Therefore, the lattice strength is given by

$$\sigma_{zz}^{pk} = \frac{2\sqrt{2}t^2}{A}\sigma_c \tag{A-11}$$

Eq. (A-11) can be expressed in terms of the relative compressive strength of the lattice as

$$\frac{\sigma_{zz}^{pk}}{\sigma_{ys}} = \frac{2\sqrt{2}t^2\sigma_c}{\sigma_{ys}A} = K_\sigma\frac{\sigma_c}{A} \tag{A-12}$$

where K_σ is a constant $=\frac{2\sqrt{2}t^2}{\sigma_{ys}}$, σ_{ys} is the yield strength of the solid material.

B.2. (001) in-plane shear

B.2.1. (001) in-plane shear modulus

Consider the octahedral cell sketched in Fig. A1(a) with an applied in-plane shear displacement δ' applied to the top node of the octahedral cell in the direction defined by an angle α ($0° \leqslant \alpha \leqslant 45°$, due to symmetry). Such a displacement can be resolved into two components perpendicular to each other as;

$$\delta'_x = \delta'\cos\alpha \tag{A-13a}$$

and

$$\delta'_y = \delta'\sin\alpha \tag{A-13b}$$

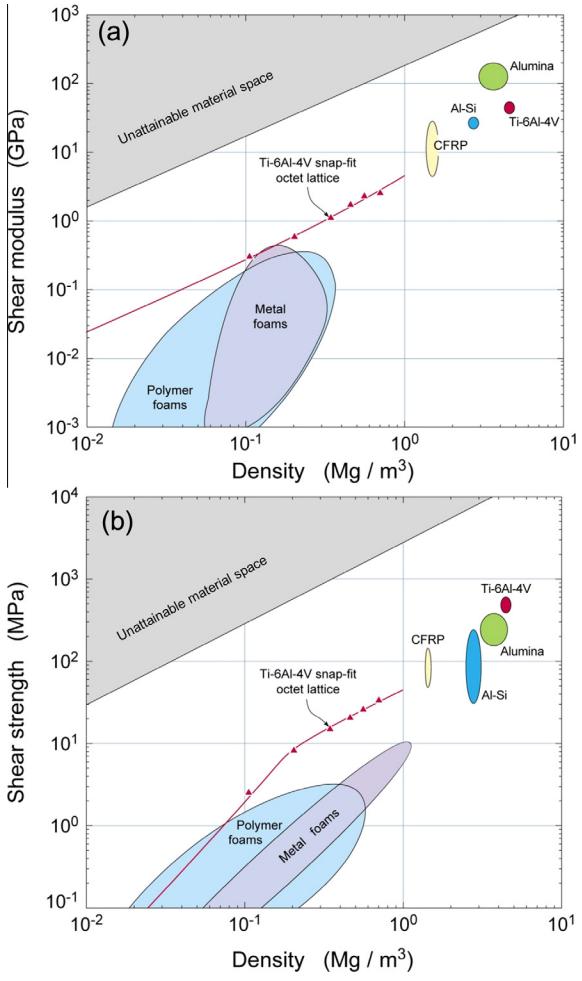

Fig. 16. Material property charts showing (a) the shear modulus and (b) the shear strength experimental data (45° Type I) and model predictions (solid curves) for the snap-fit Ti–6Al–4V octet lattices investigated here. The shear properties of polymer and metal foams and several solid materials are also shown for comparison.

Fig. A1(c) shows an edge clamped strut with length of l and side length t (width equals to length) and its free body diagram representing a single out-of-plane strut of an octahedral cell. Symmetry condition dictates that displacements and rotations of nodes apart from the top and bottom shown in Fig. A1(a) are constrained. The axial and shear displacements applied to the strut within the plane parallel to the δ'_x direction are;

$$\delta'_a = \delta'_x \cos\omega \tag{A-14a}$$

and

$$\delta'_s = \delta'_x \sin\omega \tag{A-14b}$$

with such a strut subjected to either compression or tensile displacement. According to elementary beam theory, the axial and shear forces in such a strut are given by

$$F'_A = E_s t^2 \frac{\delta'_x \cos\omega}{l} \tag{A-15a}$$

and

$$F'_S = \frac{12 E_s I \delta'_x \sin\omega}{l^3} \tag{A-15b}$$

The total force applied along the δ'_x direction of a unit cell is

$$F'_x = 2\left(F'_A \cos\omega + F'_S \sin\omega\right) = \frac{E_s t^2 \delta'_x}{l}\left[1 + \left(\frac{t}{l}\right)^2\right] \tag{A-16a}$$

The force applied along the δ'_y direction is;

$$F'_y = 2\left(F'_A \cos\omega + F'_S \sin\omega\right) = \frac{E_s t^2 \delta'_y}{l}\left[1 + \left(\frac{t}{l}\right)^2\right] \tag{A-16b}$$

It is noted that Eq. (A-16) was derived assuming fixed-end (built-in) struts ($k = 2$); for pin-joined struts ($k = 1$), the contribution to the stiffness due to the bending of the struts is negligible, and the $(t/l)^2$ related terms (i.e., F'_S terms) in Eq. (A-16) disappear, and the total shear force, F', applied on the unit cell is then

$$F' = \sqrt{F'^2_x + F'^2_y} = \frac{E_s t^2 \delta'}{l} \tag{A-17}$$

The total shear stress applied on the unit cell is thus

$$\tau = \frac{F'}{A} = \frac{E_s t^2 \delta'}{Al} \tag{A-18}$$

The shear strain

$$\gamma = \frac{2\delta'}{H} \tag{A-19}$$

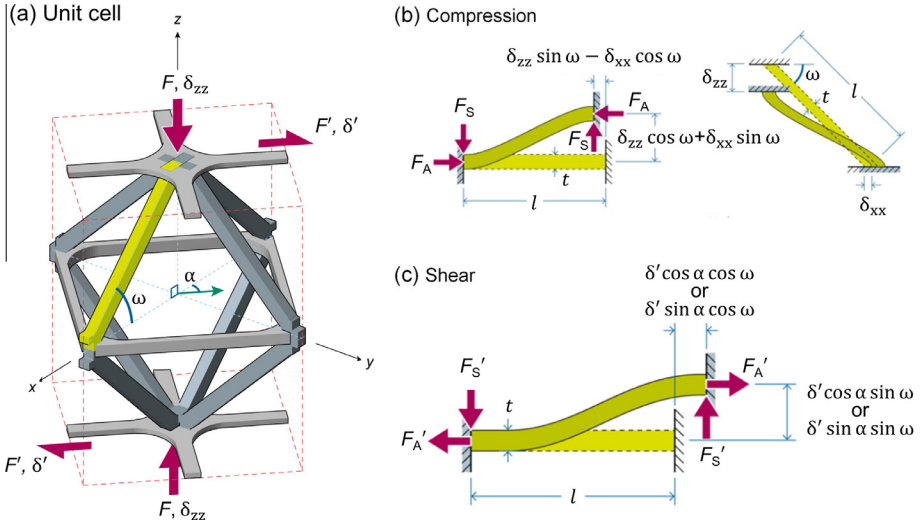

Fig. A1. Sketch of the deformation of a single out-of-plane strut under uniaxial compression and in shear. Free body diagram for such a strut showing the combination of axial and shear forces present when the unit cell is under uniaxial free compression (b) or in shear (c).

Therefore, the shear modulus of the lattice is

$$G = \frac{\tau}{\gamma} = \frac{t^2 H}{2Al} E_s \tag{A-20}$$

Eq. (A-20) can be expressed in terms of the (001) in-plane relative shear modulus as

$$\frac{G}{E_s} = \frac{t^2 H}{2Al} = K_{el} \frac{H}{Al} \tag{A-21}$$

with $K_{el} = \frac{1}{2} t^2$.

B.2.2. (001) in-plane shear strength

Eq. (A-18)represents the total shear stress applied on the unit cell ((001) in-plane shear). The axial stress in an out-of-plane strut is given by

$$\sigma_A = \frac{E_s \delta' \cos\alpha}{\sqrt{2} l} \tag{A-22}$$

Therefore, the (001) in-plane shear stress applied to the octahedral cell, τ, can be expressed in terms of the axial stress, σ_A, in an out-of-plane strut;

$$\tau = \sigma_A \frac{\sqrt{2} t^2}{A \cos\alpha} \tag{A-23}$$

The out-of-plane strut can support load until its collapse strength σ_c is achieved. Therefore, the lattice shear strength is given by

$$\tau_{pk} = \sigma_c \frac{\sqrt{2} t^2}{A \cos\alpha} \tag{A-24}$$

Eq. (A-24) can be expressed in terms of the (001) in-plane relative shear strength of the lattice as

$$\frac{\tau_{pk}}{\sigma_{ys}} = \frac{\sqrt{2} t^2}{\sigma_{ys} \cos\alpha} \frac{\sigma_c}{A} = K_\tau \frac{\sigma_c}{A} \tag{A-25}$$

where K_τ is a constant $= \frac{\sqrt{2} t^2}{\sigma_{ys} \cos\alpha}$.

Appendix C. Brazed joint minimum shear strength prediction

For the octahedral cell shown in Fig. 4(c), the contact area of pyramidal struts with the intermediate layer at a node is given by;

$$A_{\text{node}} = 2bt - t^2 \tag{A-26}$$

Eq. (A-24) indicates that the peak shear force applied to the octahedral cell is

$$\tau_{pk} A = \sigma_c \frac{\sqrt{2} t^2}{\cos\alpha} \tag{A-27}$$

To avoid node shear fracture dominated behavior, the brazed joint requires a sufficient shear strength to prevent node shear fracture prior to the attainment of peak stress under (001) in-plane shear. The minimum shear strength required for the brazed joint, τ_{braze} is therefore,

$$\tau_{\text{braze}} A_{\text{node}} \geqslant \tau_{pk} A = \sigma_c \frac{\sqrt{2} t^2}{\cos\alpha} \tag{A-28}$$

When $\alpha = 45^\circ$,

$$\tau_{\text{braze}} \geqslant \sigma_c \frac{2t}{2b - t} \tag{A-29}$$

If we conservatively take $\sigma_c = 1.1$ GPa (see Fig. 9) as the collapse strength of a single solid strut (an upper limit for σ_c), $\tau_{\text{braze}} \geqslant 440$ MPa. The measured shear strength of the brazed joint was 450 MPa; just sufficient to prevent node shear fracture becoming the dominate failure mechanism for the shear samples manufactured and tested here.

It is also noted that, the node area ($2bt - t^2$) used for the calculation above is an overly conservative estimate of brazed joint surface area (i.e. the trusses contact area) at a node. In reality, the brazed joint surface area at a node is larger ($6bt - t^2$), as the intermediate layer struts also meet the pyramidal struts at this node.

References

Adams, D.F., 2007. Shear testing of sandwich panel core materials. High-Performance Compos. 15, 8–9.

Ashby, M.F., 2000. Metal Foams: A Design Guide. Butterworth-Heinemann.

Bauer, Jens, Hengsbach, Stefan, Tesari, Iwiza, Schwaiger, Ruth, Kraft, Oliver, 2014. High-strength cellular ceramic composites with 3D microarchitecture. Proc. Natl. Acad. Sci. 111, 2453–2458.

Bitzer, T., 1997. Honeycomb technology. Chapman & Hall, London.

Boomsma, K., Poulikakos, D., Zwick, F., 2003. Metal foams as compact high performance heat exchangers. Mech. Mater. 35, 1161–1176.

Botstein, O., Rabinkin, A., 1994. Brazing of titanium-based alloys with amorphous 25wt.% Ti-25wt.% Zr-50wt.% Cu filler metal. Mater. Sci. Eng., A 188, 305–315.

Boyer, R.R., Briggs, R.D., 2005. The use of β titanium alloys in the aerospace industry. J. Mater. Eng. Perform. 14 (6), 681–685.

Boyer, R., Collings, E.W. (Eds.), 1993. Materials Properties Handbook: Titanium Alloys. ASM International.

Brewer, W.D., Bird, R.K., Terryl, A.W., 1998. Titanium alloys and processing for high speed aircraft. Mater. Sci. Eng., A 243, 299–304.

Cheung, K.C., Gershenfeld, N., 2013. Reversibly assembled cellular composite materials. Science 341, 1219–1221.

Chu, J., Engelbrecht, S., Graf, G., Rosen, D.W., 2010. A comparison of synthesis methods for cellular structures with application to additive manufacturing. Rapid Prototyping J. 16, 275–283.

Couper, J.R., Penney, W.R., Fair, J.R., 2009. Chemical Process Equipment revised 2nd Edition: Selection and Design, second ed. Gulf Professional Publishing.

Deshpande, V.S., Ashby, M.F., Fleck, N.A., 2001. Foam topology: bending versus stretching dominated architectures. Acta Mater. 49, 1035–1040.

Deshpande, V.S., Fleck, N.A., Ashby, M.F., 2001. Effective properties of the octet-truss lattice material. J. Mech. Phys. Solids 49, 1747–1769.

Dharmasena, Kumar P., Wadley, Haydn N.G., Xue, Zhenyu, Hutchinson, John W., 2008. Mechanical response of metallic honeycomb sandwich panel structures to high-intensity dynamic loading. Int. J. Impact Eng. 35, 1063–1074.

Donachie, M.J., 2000. Titanium: A Technical Guide. ASM International.

Finnegan, K., Kooistra, G., Wadley, H.N., Deshpande, V.S., 2007. The compressive response of carbon fiber composite pyramidal truss sandwich cores. Int. J. Mater. Res. 98, 1264–1272.

Froes, F.H., Friedrich, H., Kiese, J., Bergoint, D., 2004. Titanium in the family automobile: the cost challenge. JOM 56, 40–44.

Fuller, R.B., 1961, Octet Truss. U.S. Patent No. 2,986,241.

Gere, J.M., Timoshenko, S.P., 1984. Mechanics of Materials. PWS Engineering, Boston.

Gibson, L.J., Ashby, M.F., 1999. Cellular Solids: Structure and Properties. Cambridge University Press.

Gorynin, I.V., 1999. Titanium alloys for marine application. Mater. Sci. Eng., A 263, 112–116.

Holloman, Ryan, Deshpande, Vikram, Hanssen, Arve, Fleming, Katherine, Scully, John, Wadley, Haydn, 2013. Tubular aluminum cellular structures: fabrication and mechanical response. J. Mech. Mater. Struct. 8, 65–94.

Kooistra, Gregory W., Deshpande, Vikram S., Wadley, Haydn N.G., 2004. Compressive behavior of age hardenable tetrahedral lattice truss structures made from aluminium. Acta Mater. 52, 4229–4237.

Kooistra, Gregory W., Wadley, Haydn N.G., 2007. Lattice truss structures from expanded metal sheet. Mater. Des. 28, 507–514.

Kulekci, M.K., 2008. Magnesium and its alloys applications in automotive industry. Int. J. Adv. Manuf. Technol. 39, 851–865.

Lee, Yong-Hyun, Lee, Byung-Kon, Jeon, Insu, Kang, Ki-Ju, 2007. Wire-woven bulk Kagome truss cores. Acta Mater. 55, 6084–6094.

Li, Q., Chen, Y.C.E.Y., Douglas, R.B., Dunand, D.C., 2008a. Mechanical properties of cast Ti–6Al–4V lattice block structures. Metall. Mater. Trans. A 39, 441–449.

Li, Q., Chen, Y.C.E.Y., Douglas, R.B., Dunand, D.C., 2008b. Mechanical properties of cast Ti–6Al–2Sn–4Zr–2Mo lattice block structures. Adv. Eng. Mater. 10, 939–942.

Lim, Ji-Hyun, Kang, Ki-Ju, 2006. Mechanical behavior of sandwich panels with tetrahedral and Kagome truss cores fabricated from wires. Int. J. Solids Struct. 43, 5228–5246.

Lu, T.J., Stone, H.A., Ashby, M.F., 1998. Heat transfer in open-cell metal foams. Acta Mater. 46, 3619–3635.

Lugscheider, E., Broich, U., 1995 May. Mechanical properties of high-temperature brazed titanium materials, American Welding Society, Welding Research Supplement, pp. 169–176.

Onzawa, T., Suzumura, A., Ko, M.W., 1990. Brazing of titanium using low-melting-point Ti-based filler metals. Weld. J. 69, 462–467.

Park, J.S., Joo, J.H., Lee, B.C., Kang, K.J., 2011. Mechanical behaviour of tube-woven Kagome truss cores under compression. Int. J. Mech. Sci. 53 (1), 65–73.
Queheillalt, Douglas T., Wadley, Haydn N.G., 2005. Pyramidal lattice truss structures with hollow trusses. Mater. Sci. Eng., A 397, 132–137.
Queheillalt, Douglas T., Murty, Yellapu, Wadley, Haydn N.G., 2008. Mechanical properties of an extruded pyramidal lattice truss sandwich structure. Scripta Mater. 58, 76–79.
Rasmussen, K.J.R., 2003. Full range stress strain curves for stainless steel alloys. J. Constr. Steel Res. 59, 47–61.
Ritchie, R.O., Boyce, B.L., Campbell, J.P., Roder, O., Thompson, A.W., Milligan, W.W., 1999. Thresholds for high-cycle fatigue in a turbine engine Ti–6Al–4V alloy. Int. J. Fatigue 21, 653–662.
Rosen, D.W., 2007. Computer-aided design for additive manufacturing of cellular structures. Comput.-Aided Des. Appl. 4, 585–594.
Russell, Benjamin, Deshpande, Vikram, Wadley, Haydn, 2008. Quasistatic deformation and failure modes of composite square honeycombs. J. Mech. Mater. Struct. 3, 1315–1340.
SanMarchi, C., Mortensen, A., 2002. Handbook of Cellular Metals. Wiley-VCH Verlag, Weinheim Germany.
Shanley, F.R., 1967. Mechanics of Materials. McGraw-Hill, New York.
Sypeck, David J., Wadley, Haydn N.G., 2002. Cellular metal truss core sandwich structures. Adv. Eng. Mater. 4, 759–764.
Torrents, A., Schaedler, T.A., Jacobsen, A.J., Carter, W.B., Valdevit, L., 2012. Characterization of nickel-based microlattice materials with structural hierarchy from the nanometer to the millimeter scale. Acta Mater. 60, 3511–3523.
Wadley, Haydn N.G., Fleck, Norman A., Evans, Anthony G., 2003. Fabrication and structural performance of periodic cellular metal sandwich structures. Compos. Sci. Technol. 63, 2331–2343.
Wadley, Haydn N.G., 2006. Multifunctional periodic cellular metals. Philos. Trans. R. Soc. A: Math. Phys. Eng. Sci. 364, 31–68.
Wang, J., Evans, A.G., Dharmasena, K., Wadley, H.N.G., 2003. On the performance of truss panels with Kagome cores. Int. J. Solids Struct. 40, 6981–6988.
Williams, C.B., Cochran, J.K., Rosen, D.W., 2011. Additive manufacturing of metallic cellular materials via three-dimensional printing. Int. J. Adv. Manuf. Technol. 53, 231–239.
Ye, H., 2003. An overview of the development of Al–Si-alloy based material for engine applications. J. Mater. Eng. Perform. 12, 288–297.
Zheng, Xiaoyu, Lee, Howon, Weisgraber, Todd H., Shusteff, Maxim, Deotte, Joshua R., Duoss, Eric, Kuntz, Joshua D., et al., 2014. Ultra-light, ultra-stiff mechanical metamaterials. Science 344, 1373–1377.